Dysregulation of Rho GTPases in the Pix/Arhgef6 mouse model of X-linked intellectual disability is paralleled by impaired structural and synaptic plasticity and cognitive deficits

Ramakers, G J A ; Wolfer, D ; Rosenberger, G ; Kuchenbecker, K ; Kreienkamp, H J ; Prange-Kiel, J ; Rune, G ; Richter, K ; Langnaese, K ; Masneuf, S ; Bösl, M R ; Fischer, K D ; Krugers, H J ; Lipp, H P ; van Galen, E ; Kutsche, K

Abstract: Mutations in the ARHGEF6 gene, encoding the guanine nucleotide exchange factor PIX/Cool-2 for the Rho GTPases Rac1 and Cdc42, cause X-linked intellectual disability (ID) in humans. We show here that Pix/Arhgef6 is primarily expressed in neuropil regions of the hippocampus. To study the role of Pix/Arhgef6 in neuronal development and plasticity and gain insight into the pathogenic mechanisms underlying ID, we generated Pix/Arhgef6-deficient mice. Gross brain structure in these mice appeared to be normal; however, analysis of Golgi-Cox-stained pyramidal neurons revealed an increase in both dendritic length and spine density in the hippocampus, accompanied by an overall loss in spine synapses. Early-phase long-term potentiation was reduced and long-term depression was increased in the CA1 hippocampal area of Pix/Arhgef6-deficient animals. Knockout animals exhibited impaired spatial and complex learning and less behavioral control in mildly stressful situations, suggesting that this model mimics the human ID phenotype. The structural and electrophysiological alterations in the hippocampus were accompanied by a significant reduction in active Rac1 and Cdc42, but not RhoA. In conclusion, we suggest that imbalance in activity of different Rho GTPases may underlie altered neuronal connectivity and impaired synaptic function and cognition in Pix/Arhgef6 knockout mice.

DOI: https://doi.org/10.1093/hmg/ddr457

Human Molecular Genetics, 2012, Vol. 21, No. 2 ***268–286***
doi:10.1093/hmg/ddr457
Advance Access published on October 11, 2011

Dysregulation of Rho GTPases in the *αPix/Arhgef6* mouse model of X-linked intellectual disability is paralleled by impaired structural and synaptic plasticity and cognitive deficits

Ger J.A. Ramakers[1,2,†], David Wolfer[3,4,†], Georg Rosenberger[5,†], Kerstin Kuchenbecker[5], Hans-Jürgen Kreienkamp[5], Janine Prange-Kiel[6,‡], Gabriele Rune[6], Karin Richter[7], Kristina Langnaese[7], Sophie Masneuf[3], Michael R. Bösl[9,¶], Klaus-Dieter Fischer[7,8], Harm J. Krugers[10], Hans-Peter Lipp[2], Elly van Galen[1] and Kerstin Kutsche[5,*]

[1]Department of Neurons and Networks, Netherlands Institute for Neuroscience, an Institute of the Royal Netherlands Academy of Arts and Sciences, Amsterdam, The Netherlands, [2]Department of Developmental Psychology, Faculty of Behavioral and Social Sciences, University of Amsterdam, Amsterdam, The Netherlands, [3]Institute of Anatomy and Zurich Center for Integrative Human Physiology (ZIHP), University of Zurich, Switzerland, [4]Institute of Human Movement Sciences and Sport, ETH Zürich, Switzerland, [5]Institut für Humangenetik, Universitätsklinikum Hamburg-Eppendorf, Hamburg, Germany, [6]Institute of Anatomy I: Cellular Neurobiology, University Medical Center Hamburg-Eppendorf, Hamburg, Germany, [7]Institute of Biochemistry and Cell Biology and [8]Division of Functional Genomics and Medical Toponomics at the Centre for Cellular Imaging and Innovative Disease Models, Otto von Guericke University Magdeburg, Magdeburg, Germany, [9]Center for Molecular Neurobiology, Hamburg, Germany and [10]Swammerdam Institute for Life Sciences, Center for Neuroscience, Amsterdam, The Netherlands

Received August 26, 2011; Revised and Accepted September 29, 2011

Mutations in the *ARHGEF6* gene, encoding the guanine nucleotide exchange factor αPIX/Cool-2 for the Rho GTPases Rac1 and Cdc42, cause X-linked intellectual disability (ID) in humans. We show here that *αPix/Arhgef6* is primarily expressed in neuropil regions of the hippocampus. To study the role of αPix/Arhgef6 in neuronal development and plasticity and gain insight into the pathogenic mechanisms underlying ID, we generated *αPix/Arhgef6*-deficient mice. Gross brain structure in these mice appeared to be normal; however, analysis of Golgi-Cox-stained pyramidal neurons revealed an increase in both dendritic length and spine density in the hippocampus, accompanied by an overall loss in spine synapses. Early-phase long-term potentiation was reduced and long-term depression was increased in the CA1 hippocampal area of *αPix/Arhgef6*-deficient animals. Knockout animals exhibited impaired spatial and complex learning and less behavioral control in mildly stressful situations, suggesting that this model mimics the human ID phenotype. The structural and electrophysiological alterations in the hippocampus were accompanied by a significant reduction in active Rac1 and Cdc42, but not RhoA. In conclusion, we suggest that imbalance in activity of different Rho GTPases may underlie altered neuronal connectivity and impaired synaptic function and cognition in *αPix/Arhgef6* knockout mice.

*To whom correspondence should be addressed at: Institut für Humangenetik, Universitätsklinikum Hamburg-Eppendorf, Campus Forschung, Martinistraße 52, 20246 Hamburg, Germany. Tel: +49 40741054597; Fax: +49 40741055138; Email: kkutsche@uke.de
†The authors wish it to be known that, in their opinion, the first three authors should be regarded as joint First Authors.
‡Present address: Department of Cell Biology, University of Texas, Southwestern Medical Center at Dallas, Texas, USA.
¶Present address: MPI of Neurobiology, Martinsried, Germany.

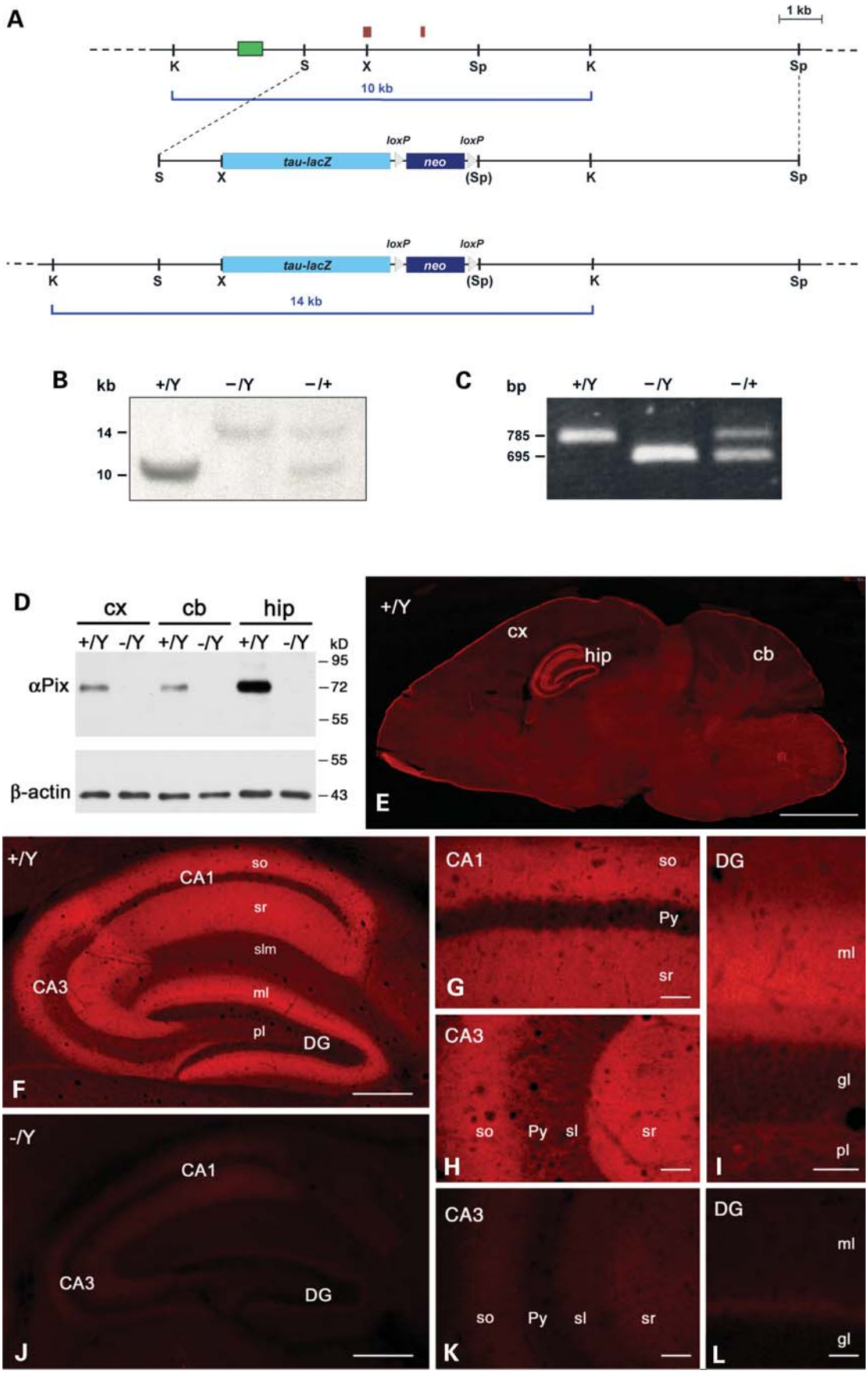

INTRODUCTION

Rho GTPases belong to the family of small GTPases which act as molecular switches by cycling between an active, GTP-bound and an inactive, GDP-bound state. The activity state of Rho GTPases is tightly controlled by positive and negative regulators. Guanine nucleotide exchange factors (GEFs) activate Rho proteins by mediating the exchange of GDP for GTP (1), whereas GTPase-activating proteins (GAPs) stimulate the low intrinsic GTP hydrolysis rate (2), thereby negatively regulating Rho signaling. In the active state, Rho GTPases exert their effect on various cellular functions. The most extensively studied Rho GTPases Rac1, Cdc42 and RhoA are best known for their role in controlling dynamics of the actin cytoskeleton (3,4). Because actin filaments make up the structural framework of dendrites, axons and dendritic spines, Rho signaling pathways have been suggested to be critically important for neurite outgrowth and branching, axon pathfinding and dendritic spine morphogenesis (5–9).

The importance of Rho-dependent signaling in neuronal development and function has been highlighted by the identification of mutations in Rho-linked genes causing intellectual disability (ID) in humans (10–12). ID is the most common developmental disability in children and is defined by a global deficiency of cognitive abilities and adaptive skills (13). It has been proposed that patients with ID show a deficit in neuronal network connectivity, resulting in abnormal information processing (14). There is evidence that the cerebral cortex and the hippocampus are structurally altered in ID, although the underlying mechanisms are not completely understood (15,16). Mutations in five genes, *FGD1*, *OPHN1*, *PAK3*, *ARHGEF9* and *ARHGEF6* (also known as *αPIX* or *Cool-2*), encoding proteins directly interacting with Rho GTPases, have been identified in patients with X-linked ID (17–23). The GAP oligophrenin-1 (OPHN1) negatively regulates RhoA, Rac1 and Cdc42 (18). PAK3 is a member of the large family of p21-activating kinases (PAK), acting as downstream effectors of Rac1 and Cdc42 (24). FGD1, ARHGEF9 (collybistin) and αPIX/ARHGEF6 are GEFs; collybistin and FGD1 are specific for Cdc42 (25,26), while αPIX/ARHGEF6 activates both Rac1 and Cdc42 (27). Of note, exchange activity of αPix/Arhgef6 has so far been demonstrated only *in vitro* and underlies a complex allosteric regulation (28–34).

αPix/Arhgef6 transcripts have been detected in rat hippocampal CA1–CA3 cell layers and ectopically expressed αPix/Arhgef6 colocalizes with postsynaptic density (PSD) -95 at postsynaptic densities of excitatory synapses in cultured neurons (35). Knockdown of *αPix/Arhgef6* results in abnormal spine morphology in hippocampal organotypic slice cultures. The active form of Pak3 rescues the phenotype induced by *αPix/Arhgef6* downregulation, suggesting that αPix/Arhgef6 acts upstream of Pak3 in regulating spine morphogenesis and plasticity of synaptic networks (35).

To establish the role of the X-linked ID gene *αPIX/ARHGEF6 in vivo*, we generated and characterized constitutional *αPix/Arhgef6* knockout mice. As we found αPix/Arhgef6 to be highly expressed in the hippocampal formation and the hippocampus has a major role in learning and memory (36), we studied synaptic morphology and long-term potentiation (LTP) as well as hippocampus-dependent cognitive behavior in *αPix/Arhgef6*-deficient mice.

RESULTS

αPix/Arhgef6$^{-/Y}$ mice are viable and show no changes in gross brain morphology

The targeting strategy for *αPix/Arhgef6* knockout mice was designed to abolish expression of αPix/Arhgef6 resulting in a functional null allele (Fig. 1A). Backcrosses into the C57BL/6 genetic background were done and the N6 to N12 generations were used in the majority of tests. Genotype of animals from the N2 generation was analyzed by Southern blot (Fig. 1B), whereas for all subsequent generations we determined the genotype by multiplex polymerase chain reaction (PCR) (Fig. 1C). Breeding heterozygous females with wild-type C57BL/6 males resulted in offspring in the expected Mendelian segregation ratio of an X-chromosomal allele indicating that, as in humans, the murine *αPix/Arhgef6* gene is not essential for life. Only male *αPix/Arhgef6* knockout offspring (*αPix/Arhgef6*$^{-/Y}$) and their wild-type littermates (*αPix/Arhgef6*$^{+/Y}$) were investigated in the present study. *αPix/Arhgef6*$^{-/Y}$ animals showed no apparent changes in viability, lifespan and

Figure 1. Generation of *αPix/Arhgef6*$^{-/Y}$ mice and high abundance of αPix/Arhgef6 in neuropil regions of the hippocampal formation. (**A**) Schematic representation of the wild-type *αPix/Arhgef6* allele (top), targeting vector (middle), and targeted allele after homologous recombination (bottom). Red boxes indicate *αPix/Arhgef6* exons 1 and 2, the green box represents the location of the SB3 probe used for Southern blotting, the light blue box the *tau-lacZ* gene, the dark blue box the neomycin cassette and grey arrowheads *lox*P sites. K, *Kpn*I; S, *Sph*I; Sp, *Spe*I, (Sp), destroyed *Spe*I site; X, *Xba*I. (**B**) Southern blot analysis of tail DNA prepared from male (+/Y and −/Y) and female (−/+) offspring. Genomic DNA was digested with *Kpn*I and probed with the 5′ external probe SB3. Wild-type and mutant alleles generated fragments of 10 and 14 kb, respectively. (**C**) Multiplex PCR analysis on tail DNA prepared from wild-type (+/Y), knockout (−/Y) and heterozygous mice (−/+). A 785 bp amplicon was generated from the wild-type allele, while a PCR product of 695 bp was amplified from the targeted *αPix/Arhgef6* allele. (**D**) Immunoblotting showed that the ∼72 kDa αPix/Arhgef6 protein was strongly expressed in hippocampal lysates and moderately in cortical and cerebellar lysates from adult wild-type (+/Y), but not from *αPix/Arhgef6*$^{-/Y}$ (−/Y) mice. Equal protein loading was confirmed by probing with an anti-actin antibody. (**E** and **F**) Sagital sections of a wild-type (+/Y) mouse brain revealed a distinct expression of αPix/Arhgef6 in the hippocampal formation. The stratum oriens and stratum radiatum of the CA1–CA3 region (**G** and **H**) and the inner molecular layer of the dentate gyrus (**I**) showed dense immunolabeling. The pyramidal cell layer and the stratum lucidum of the CA3 region (H), the stratum lacunosum-moleculare of the CA1 region (F) as well as the polymorphic layer of the dentate gyrus (I) are only moderately stained. The pyramidal cell layers of CA1 (G) and the granule cell layer of dentate gyrus (I) showed only faint labeling. (**J**–**L**) Staining of sections from *αPix/Arhgef6*-deficient mice (−/Y) showed very weak immunoreactivity in the stratum oriens and stratum radiatum of the CA1–CA3 region, in the stratum lucidum of the CA3 region and in a small band in the molecular layer adjacent to the granule cell body layer in the dentate gyrus. CA1, CA1 region of the hippocampus; CA3, CA3 region of the hippocampus; cb, cerebellum; cx, cortex; DG, dentate gyrus; gl, granule cell layer; hip, hippocampus; ml, molecular layer; pl, polymorphic layer; Py, pyramidal cell layer; sl, stratum lucidum; slm, stratum lacunosum-moleculare; so, stratum oriens; sr, stratum radiatum. Scale bars: 2 mm in (E); 200 μm in (F) and (J); 50 μm in (G–I), (K) and (L). Age of mice used in the experiments was 12–15 weeks.

fertility. Histological analysis of hematoxylin–eosin-stained and Nissl-stained, fixed brain sections revealed no obvious abnormalities in gross anatomy of the CNS, including hippocampus and cerebellum of *αPix/Arhgef6*$^{-/Y}$ mice (data not shown).

αPix/Arhgef6 is expressed in neuropil areas of the hippocampus

αPix/Arhgef6 mRNA expression in the brain has been described before (35,37); however, the protein expression pattern in various brain areas is largely unknown. Therefore, we performed immunoblot analysis of protein lysates derived from different brain areas of adult wild-type mice using a specific anti-αPix/Arhgef6 antibody. We observed high levels of the ∼72 kDa αPix/Arhgef6 isoform in the hippocampus and lower levels in the cortex and cerebellum (Fig. 1D). αPix/Arhgef6 was absent in lysates derived from *αPix/Arhgef6*$^{-/Y}$ mice (Fig. 1D). To confirm robust expression of αPix/Arhgef6 specifically in the hippocampus, we investigated its spatial distribution in the mouse brain by immunofluorescence microscopy. Again, low immunoreactivity was detected throughout the brain, with the exception of the hippocampal formation (Fig. 1E), where strong αPix/Arhgef6 immunoreactivity was observed in neuropil areas (Fig. 1F–I and data not shown). In particular, the stratum radiatum and stratum oriens of the CA1–CA3 region showed an intense labeling (Fig. 1F–H), whereas the stratum lacunosum-moleculare and stratum lucidum were only moderately stained (Fig. 1F and H). The molecular layer of the dentate gyrus was characterized by a bipartite staining pattern with strong immunoreactivity in its proximal part and a moderate staining in its distal areas, in the vicinity of the stratum lacunosum-moleculare (Fig. 1F and I). The perikarya of pyramidal cells of CA1 as well as granule cells of the dentate gyrus were almost unstained (Fig. 1G and I), whereas the cell bodies of CA3 pyramidal cells and the polymorphic cell layer of the dentate gyrus were moderately labeled (Fig. 1H and I). Only background immunoreactivity was found in sections from *αPix/Arhgef6*$^{-/Y}$ mice (Fig. 1J–L). Equal staining of neuronal cell bodies and dendrites in the hippocampus of wild-type and *αPix/Arhgef6*$^{-/Y}$ mice was observed with an anti-MAP2 antibody (Supplementary Material, Fig. S1). In summary, αPix/Arhgef6 showed a strong expression in the adult hippocampus, with a dense localization in neuropil regions.

Loss of αPix/Arhgef6 results in reduced levels of active Rac1 and Cdc42 in the hippocampus and subtle changes in the expression of cytoskeletal regulators

The activity of Rho GTPases has been implicated in different aspects of neuronal morphogenesis (5). Since αPix/Arhgef6 stimulates the activation of Cdc42 and Rac1 (27–34), we determined the amount of active, GTP-bound Rac1 and Cdc42 in brain lysates from 3-month-old wild-type and *αPix/Arhgef6*$^{-/Y}$ animals by GTPase activation assays. We detected slightly reduced levels of activated Cdc42 and Rac1 in *αPix/Arhgef6*$^{-/Y}$ animals (Fig. 2A). By studying different brain regions, we observed decreased active Rac1 and Cdc42 in the hippocampus of *αPix/Arhgef6*$^{-/Y}$ mice, whereas the level of GTP-bound Rac1 and Cdc42 in the neocortex and cerebellum was similar to that of wild-type mice (Fig. 2B). The decrease in Rho GTPase activation seems to be specific for Rac1 and Cdc42 in *αPix/Arhgef6*$^{-/Y}$ animals as activation of RhoA was the same in the hippocampus of wild-type and *αPix/Arhgef6*$^{-/Y}$ animals (Fig. 2C). Densitometric measurement of autoradiographs followed by statistical analysis revealed an average decrease in active Cdc42 to 77% ($\pm$7.8%; $P < 0.05$) and active Rac1 to 79% ($\pm$5.6%; $P < 0.01$) in hippocampus lysates of *αPix/Arhgef6*$^{-/Y}$ animals compared with wild-type levels (Fig. 2D). These data indicate that the loss of αPix/Arhgef6 is associated with a significant decrease in active Cdc42 and Rac1, but not RhoA, in the hippocampus *in vivo*.

Due to the prominent role of Cdc42 and Rac1 in cytoskeletal reorganization, we analyzed expression and/or activation of various regulators of the actin cytoskeleton and αPix/Arhgef6 protein–protein interaction partners in hippocampal lysates from *αPix/Arhgef6*$^{-/Y}$ and wild-type animals. Protein levels of the αPix/Arhgef6 binding proteins Cbl-b, Git1 and 2, and βPix were unchanged in *αPix/Arhgef6*$^{-/Y}$ mice, those of the cytoskeletal regulators Pak1-3, Limk1 and Cofilin were slightly increased (Supplementary Material, Fig. S2). Relative phosphorylation of Pak1/2, Pak3, Limk1 and Cofilin in *αPix/Arhgef6*$^{-/Y}$ mice, however, was comparable to wild-type animals (Supplementary Material, Fig. S2). Taken together, *αPix/Arhgef6* deficiency is accompanied by a subtle increase in the amount of some cytoskeletal regulator proteins, which may potentially act downstream of αPix/Arhgef6.

Changes in dendritic morphology and linear spine density in hippocampal area CA1 of *αPix/Arhgef6*$^{-/Y}$ mice

Next, we analyzed the cytoarchitecture of the hippocampus by analysis of randomly selected Golgi-stained pyramidal neurons from area CA1 of 12-week-old wild-type and *αPix/Arhgef6*$^{-/Y}$ animals (Supplementary Material, Fig. S3). The total dendrite length per neuron was increased by 16% in *αPix/Arhgef6*$^{-/Y}$ mice ($P < 0.05$) (Fig. 3A). This increase was completely attributed to longer dendrites and not to changes in the number of dendrites per neuron (Supplementary Material, Fig. S4). The length of apical and basal dendrites was increased by 21 and 34% in *αPix/Arhgef6*$^{-/Y}$ mice, respectively ($P < 0.01$ for apical dendrites; $P < 0.001$ for basal dendrites) (Fig. 3B and F). We also found an increase in the number of branch points per dendrite, by 24% for apical and 28% for basal dendrites (both $P < 0.001$) (Fig. 3C and G). For apical dendrites, the intermediate and terminal segment lengths were unchanged (Fig. 3D and E), while for basal dendrites, only the length of the terminal segments was increased by 10% ($P < 0.001$) (Fig. 3H and I).

In 8-week-old mice, we observed similar changes: the total dendrite length per neuron was increased by 35% ($P < 0.05$) (Supplementary Material, Fig. S5). This increase was due to moderate increases in the number of dendrites per neuron (by 14%; data not shown), apical dendrite length (by 13%) and basal dendrite length (by 13%; $P = 0.058$), all of which failed to reach significance (Supplementary Material, Fig. S5). However, both apical and basal dendrites showed a significant increase in terminal segment length (by 22% and

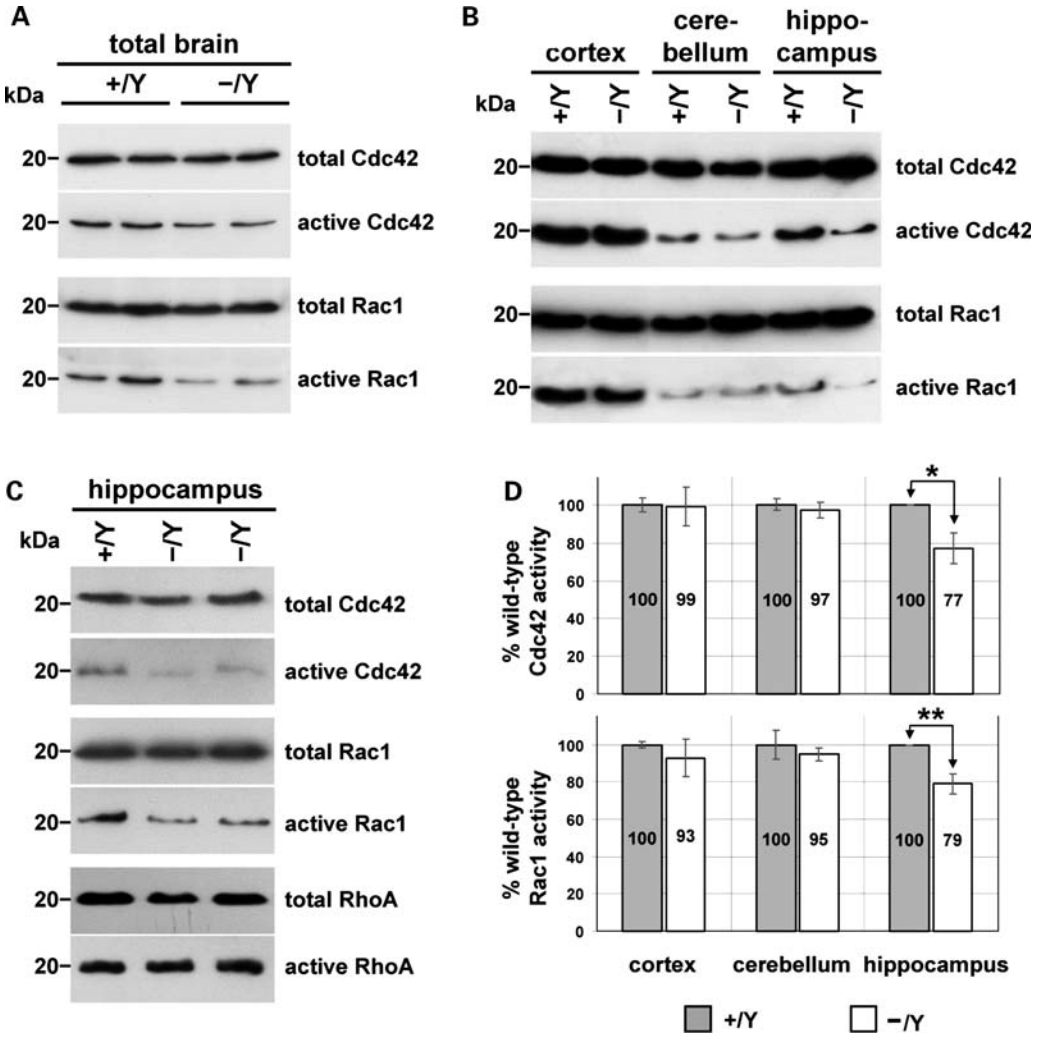

Figure 2. Loss of αPix/Arhgef6 results in decreased levels of active Rac1 and Cdc42. (**A**) GTPase activity assays revealed slightly reduced amounts of GTP-bound Cdc42 and Rac1 in total brain lysates of 3-month-old *αPix/Arhgef6*$^{-/Y}$ mice (−/Y) compared with wild-type animals (+/Y). GTP-bound Rac1 and Cdc42 were pulled down from protein lysates of total brain derived from two animals per genotype using the GST-PAK[PBD] fusion protein. Precipitated (active) and total amounts (active and inactive) of Cdc42 and Rac1 were detected by immunoblotting using anti-Cdc42 and anti-Rac1 antibodies. (**B**) Levels of both activated Cdc42 and Rac1 were reduced in the hippocampus of *αPix/Arhgef6*$^{-/Y}$ mice, but not in the cortex and cerebellum. (**C**) Decreased activation is specific for Cdc42 and Rac1 in *αPix/Arhgef6*$^{-/Y}$ mice. Hippocampal lysates of two animals were pooled and then split into two aliquots. One aliquot was assayed for activation of Cdc42 and Rac1, and the other aliquot was analyzed for the level of active RhoA by using GST-Rhotekin[RBD] to trap the GTP-bound form. Levels of RhoA were detected both in precipitates and raw lysates by immunoblotting using anti-RhoA antibody. (**D**) Quantification of active Cdc42 and Rac1 by densitometric and statistical analysis. Data represent the mean of four independent experiments (each with two animals per genotype) ± SD. Activation levels of Cdc42 and Rac1 were normalized to total Cdc42 and Rac1, respectively, and are expressed as percentage of control levels (wild-type mice: +/Y). Active Cdc42 and Rac1 were significantly reduced in hippocampal lysates of *αPix/Arhgef6*$^{-/Y}$ mice (−/Y) (*$P < 0.05$; **$P < 0.01$; two-tailed Student's *t*-test), but were unchanged in cortical and cerebellar lysates ($P > 0.05$; two-tailed Student's *t*-test).

by 25%, respectively; $P < 0.01$ and $P < 0.05$, respectively) (Supplementary Material, Fig. S5). In summary, dendrite length increased in hippocampal area CA1 between 8 and 12 weeks of age of both wild-type and knockout animals. However, *αPix/Arhgef6*$^{-/Y}$ mice additionally showed an increased number of branch points (Fig. 3 and Supplementary Material, Fig. S5).

Next, we determined the number of dendritic protrusions (see Materials and Methods for classification of spines and filopodia) and found no significant difference in the linear density of spines and filopodia on basal dendrites of wild-type and mutant animals (data not shown). In contrast, on apical dendrites where the density of spines and filopodia per 20 μm of the dendrite was quantitated as a function of distance from the soma (Sholl analysis), we detected an increase in the total number of both spines (by 62%; $P < 0.05$) and filopodia (by 41%) per apical dendrite in *αPix/Arhgef6*$^{-/Y}$ mice (Supplementary Material, Fig. S6). However, the proportion of filopodia (~40% of all protrusions) was not significantly altered in *αPix/Arhgef6*$^{-/Y}$ animals (Supplementary Material, Fig. S7).

Sholl analysis also revealed elevated spine densities at several locations along the apical dendrite (Fig. 4A), while filopodia densities were not significantly increased in *αPix/Arhgef6*$^{-/Y}$ mice (Fig. 4B). We nest assessed the morphology of spines

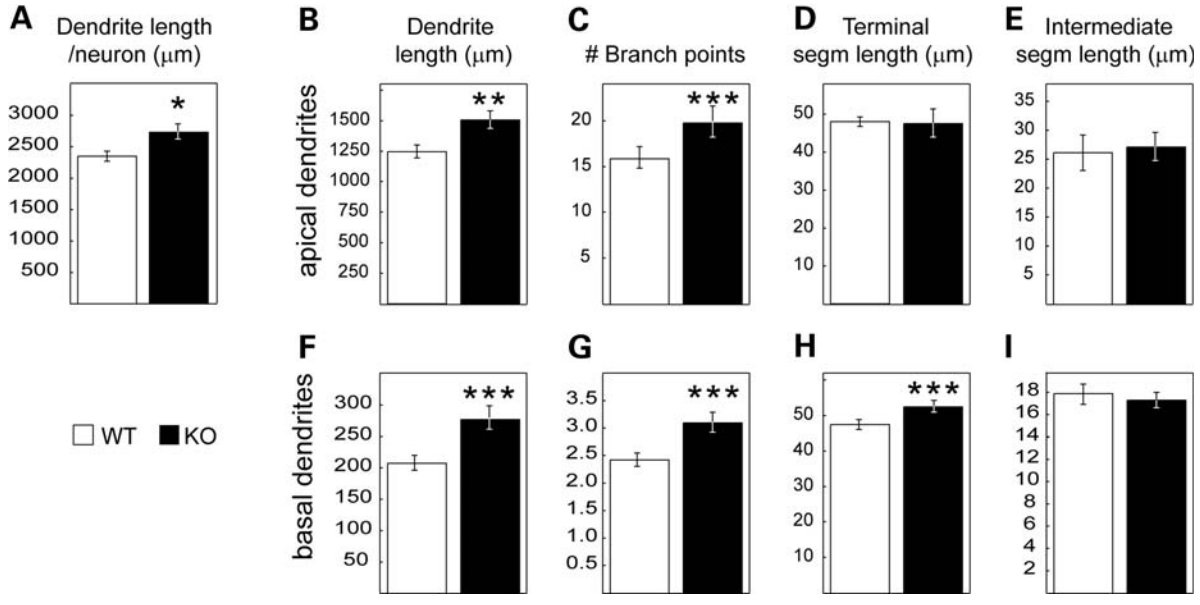

Figure 3. Altered dendritic morphology in 12-week-old *αPix/Arhgef6*$^{-/Y}$ mice. Dendritic morphology of pyramidal neurons in hippocampus CA1 of 5 *αPix/Arhgef6*$^{-/Y}$ mice and 11 wild-type littermates at the age of 12 weeks was quantified after Golgi-Cox impregnation. (**A**) Total dendrite length per neuron was increased in *αPix/Arhgef6*$^{-/Y}$ mice. (**B** and **F**) Apical and basal dendrites of *αPix/Arhgef6*$^{-/Y}$ mice were significantly longer than those of wild-type animals, mainly resulting from an increased number of branch points in both types of dendrites (**C** and **G**). The intermediate and terminal segment lengths were unchanged for apical dendrites (**D** and **E**), while for basal dendrites, the length of terminal segments was significantly increased in *αPix/Arhgef6*$^{-/Y}$ mice (**H**). For wild-type (WT): $n = 88$ apical and 461 basal dendrites; for knockout (KO): $n = 50$ apical and 225 basal dendrites. Significance is indicated ($^{*}P < 0.05$; $^{**}P < 0.01$; $^{***}P < 0.001$). Segm: segment. Error bars represent SEM.

and observed no changes in spine head diameter and width (Fig. 4C and D); however, the spine neck length was slightly (6%) but significantly increased ($P < 0.01$) in *αPix/Arhgef6*$^{-/Y}$ animals (Fig. 4E). In summary, we found longer and more branched dendrites and an increased linear density of spines in CA1 pyramidal cells of 12-week-old *αPix/Arhgef6*$^{-/Y}$ mice.

To analyze whether the increase in spine density is paralleled by an increase in spine synapses, we stereologically quantified spine synapses in the stratum radiatum of the hippocampal CA1 area (Supplementary Material, Fig. S8). Surprisingly, we found a significant loss of synapse density per unit volume by ~25% ($P < 0.05$) in *αPix/Arhgef6*$^{-/Y}$ mice from 10 weeks of age onwards, while the number of spine synapses was not altered in 3-week-old mutant mice (Fig. 5A). When we measured the total cortex and hippocampus volume (at 12 weeks of age), we did not find significant differences between mutant and wild-type animals (Fig. 5B). We also determined the total number of neurons in the pyramidal layer of the hippocampal CA1 subfield and found no difference between knockout and wild-type mice at 16 weeks of age (Fig. 5C).

Together, these data indicate that the *αPix/Arhgef6* null mutation *in vivo* produces a significant increase in the number of dendritic spines along apical dendrites of single neurons on the one hand and induces a reduction in excitatory contact density in adult mice on the other hand.

Mild alterations in dendritic morphology in *αPix/Arhgef6*$^{-/Y}$ mouse primary visual cortex

Since αPix/Arhgef6 is more abundant in hippocampus than in the cerebral cortex, we also examined whether the loss of αPix/Arhgef6 had any effect on dendritic morphology in primary visual cortex. Dendrites of pyramidal neurons from layers 5/6 were analyzed in 12-week-old wild-type and *αPix/Arhgef6*$^{-/Y}$ mice. Loss of αPix/Arhgef6 did not affect total dendrite length per neuron or any apical dendrite parameter (Supplementary Material, Fig. S9). Basal dendrites showed a modest increase in length, which resulted from a combination of mild increases in the number of branch points and in the length of terminal and intermediate segments (Supplementary Material, Fig. S9). Compared with the changes in dendritic morphology in hippocampal area CA1, dendritic alterations in primary visual cortex layer 5/6 were relatively mild that is in accordance with the lower abundance of αPix/Arhgef6 in this brain region.

Decreased LTP and increased LTD in *αPix/Arhgef6*$^{-/Y}$ mice

We also explored the physiological consequences of the structural modifications induced by loss of *αPix/Arhgef6* by investigating synaptic function in adult knockout mice and analyzed LTP and long-term depression (LTD), two well-studied electrophysiological correlates of learning and memory (38,39). We measured early-phase LTP (E-LTP) in the connections of Schaffer collaterals onto the spines of apical dendrites of area CA1 pyramidal neurons. Extracellular recording of input–output characteristics of the Schaffer collateral–CA1 pyramidal circuitry (stimulus strength versus field potential amplitude) showed no significant differences between adult knockout and wild-type animals (Supplementary Material, Fig. S10), indicating normal basal neurotransmission. In wild-type mice, a strong

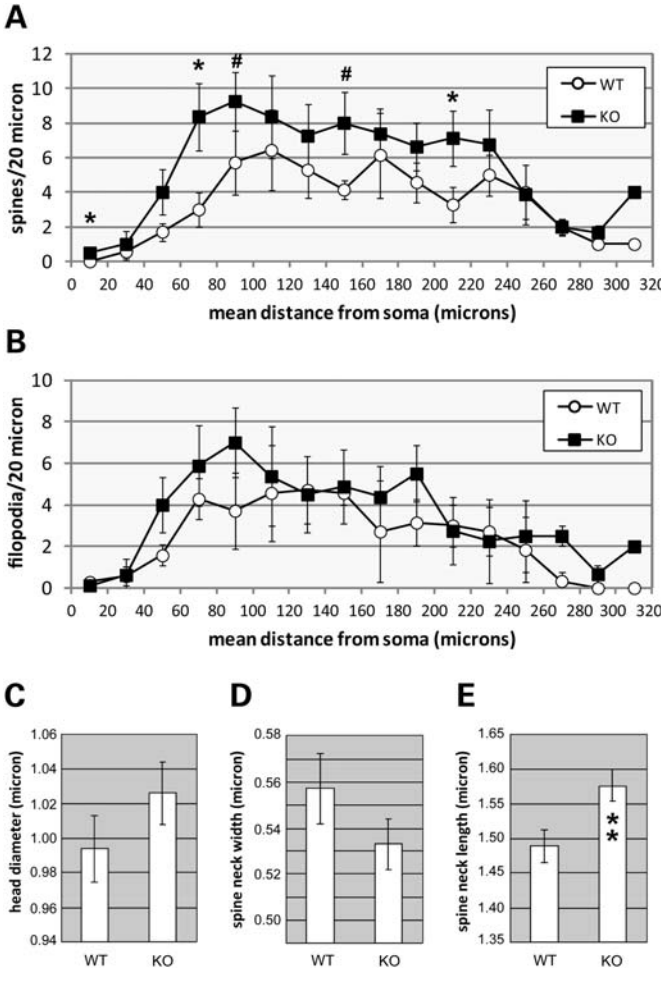

Figure 4. Increased dendritic spine density in CA1 pyramidal neurons of *αPix/Arhgef6*$^{-/Y}$ mice. (**A**) Sholl analysis of spine densities along apical dendrites. Spines (defined by the presence of a terminal head) were counted along stretches of 20 μm from the soma to the terminal tips of the dendrite. The total spine number was increased for apical dendrites of 12-week-old *αPix/Arhgef6*$^{-/Y}$ mice ($P < 0.05$; WT: $n = 7$ neurons; KO: $n = 8$ neurons; from four mice in each group). (**B**) Sholl analysis of filopodia densities along apical dendrites. Filopodia (defined by the absence of a terminal head) were counted along stretches of 20 μm from the soma to the terminal tip of the dendrite. The total filopodia number was increased for apical dendrites of *αPix/Arhgef6*$^{-/Y}$ mice ($P < 0.05$; WT: $n = 7$ neurons; KO: $n = 8$ neurons; from four mice in each group). (**C**–**E**) Diameter of the spine heads (C), spine neck width (D) and spine neck length (E) of dendritic spines measured along the apical dendrite. Spine neck length showed a significant increase in *αPix/Arhgef6*$^{-/Y}$ animals. Mann–Whitney statistics were used in all cases. Significance is indicated ($^{\#}P < 0.1$; $^{*}P < 0.05$; $^{**}P < 0.01$). WT, wild-type mice; KO, *αPix/Arhgef6*$^{-/Y}$ mice.

induction of E-LTP (+136% at 50–60 min after induction) was observed which lasted at least 1 h (Fig. 6A). In *αPix/Arhgef6*$^{-/Y}$ mice, E-LTP was also induced; however, its magnitude was significantly lower ($P < 0.05$) than in wild-type animals (+70% at 50–60 min after induction, Fig. 6A). We failed to induce LTD (after a train of 900 pulses at a frequency of 1 Hz) in wild-type mice (Fig. 6B), as commonly found in adult rodents (40–42). In contrast, we observed significant induction of LTD in *αPix/Arhgef6*$^{-/Y}$ mice (Fig. 6B). Altogether, decreased E-LTP and increased LTD indicate altered synaptic plasticity in hippocampal area CA1 of *αPix/Arhgef6*$^{-/Y}$ mice.

As alterations in synaptic plasticity may be due to alterations in the postsynaptic complement of glutamate receptors (specifically the α-amino-3-hydroxy-5-methyl-4-isoxazolepropionic acid/N-methyl D-aspartate (AMPA/NMDA) receptor ratio) (43,44), we analyzed whether the loss of αPix/Arhgef6 affected the abundance of postsynaptic ionotropic glutamate receptor subunits. To this end, we prepared the PSD from forebrains of wild-type and *αPix/Arhgef6*$^{-/Y}$ animals. PSD samples were analyzed by western blotting using antibodies directed against NMDA and AMPA receptor subunits (Supplementary Material, Fig. S11). Quantitative evaluation of blots revealed that the levels of all subunits tested were slightly increased in *αPix/Arhgef6*$^{-/Y}$ mice. Differences were statistically significant only for the Grin1/NR1 subunit of NMDA receptors. Importantly, the AMPA receptor/NMDA receptor ratio was unaltered in *αPix/Arhgef6*$^{-/Y}$ mice (Supplementary Material, Fig. S11).

αPix/Arhgef6$^{-/Y}$ mice show navigation errors and spatial perseverance in the water-maze place navigation task

We assessed the cognitive behavior of *αPix/Arhgef6*$^{-/Y}$ mice by analyzing spatial learning and memory in a water-maze place navigation procedure with a reversal phase. According to swim path length (Fig. 7A) and escape latency (Table 1), *αPix/Arhgef6*$^{-/Y}$ mice showed normal escape performance during acquisition and reversal with the goal platform placed in the opposite quadrant. Performance dropped after relocation of the goal platform in both control and mutant animals (Fig. 7A), indicating that the mice had adapted their swimming strategy to the specific goal location during acquisition. *αPix/Arhgef6*$^{-/Y}$ mice displayed as little passive floating as controls and were indistinguishable from normal mice with respect to wall hugging and tendency to swim in circles at a constant distance from the wall (chaining). There was also no indication of impaired motor performance in *αPix/Arhgef6*$^{-/Y}$ mice, as reflected by normal swim speed and unaltered scores for path tortuosity and circling (Table 1). However, more detailed analysis of swim paths revealed a strong increase in time spent in the goal quadrant and target proximity by the mutant mice (45) (Fig. 7C and Table 1). Surprisingly, this was combined with markedly impaired scores on Whishaw's error index (Table 1), a measure of how well swim paths fit into a straight corridor connecting the start point with the goal (46). Closer inspection of swim paths during late acquisition revealed frequent near misses of the goal in *αPix/Arhgef6*$^{-/Y}$ mice and a strong tendency of perseverant searching at locations near the target (Fig. 7C). During the probe trial, 24 h after completion of acquisition, both groups spent more time in the trained zone than in control zones in the adjacent quadrants, with no difference between wild-type and knockout mice (Fig. 7B). Spatial retention was also normal according to the time spent in target quadrants and number of annulus crossings (Table 1). Unlike wild-type mice, *αPix/Arhgef6*$^{-/Y}$ mice persistently searched at or near the old goal site, even on the second day of reversal (Fig. 7D). This resulted in marked differences of quadrant and zone time as well as annulus crossings between mutant and wild-type mice (Table 1).

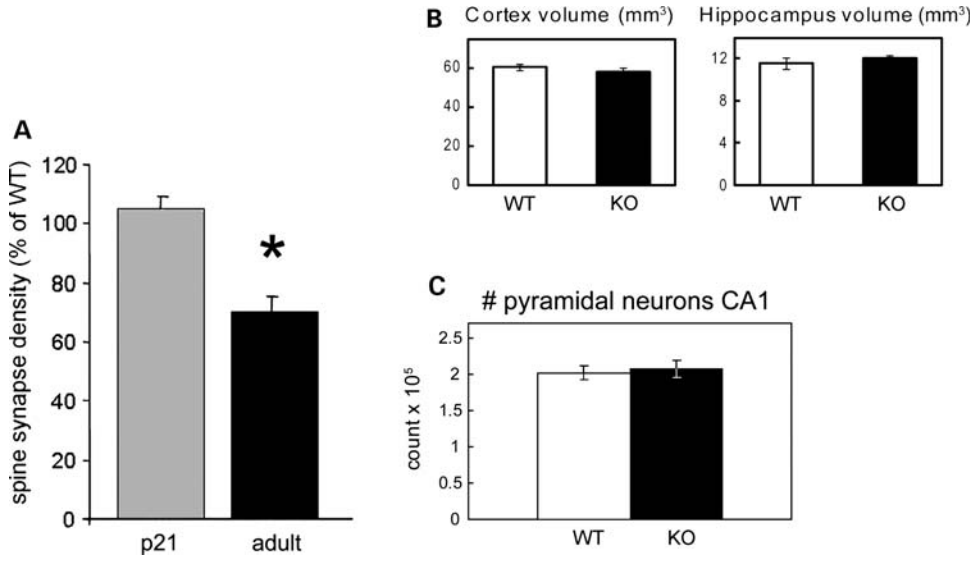

Figure 5. Synapse loss in adult *αPix/Arhgef6*$^{-/Y}$ mice. (**A**) Stereological evaluation of spine synapse density in the stratum radiatum of CA1. Counts of spine synapses in *αPix/Arhgef6*$^{-/Y}$ animals are expressed as percentage of those obtained in wild-type animals ($n = 9$). Synapse loss of ∼25% was observed in adult *αPix/Arhgef6*$^{-/Y}$ mice (10–24 weeks of age; $n = 9$), whereas younger animals (P21; $n = 3$) showed similar numbers of spine synapses as wild-type animals. Error bars represent SEM; $^{*}P < 0.05$. (**B**) The total volume of the cortex and hippocampus is unchanged in *αPix/Arhgef6*$^{-/Y}$ mice. The volume of both cortex and hippocampus of 12-week-old *αPix/Arhgef6*$^{-/Y}$ mice (KO) and wild-type littermates (WT) ($n = 4$) was estimated on Nissl-stained brain sections using the Cavalieri method (75,76). No changes were found. Error bars represent SEM. (**C**) The total number of neurons in hippocampal CA1 area of *αPix/Arhgef6*$^{-/Y}$ mice is unchanged. Neurons in the pyramidal layer of hippocampus CA1 were counted using the optical dissector method. $n = 5$ wild-type (WT) and four *αPix/Arhgef6*$^{-/Y}$ mice (KO) (all 16 weeks old). Error bars represent SEM.

Spatial working memory of *αPix/Arhgef6*$^{-/Y}$ mice, assessed on the eight-arm radial maze, was normal. Bait omissions, arm neglects and aborted arm visits of *αPix/Arhgef6*$^{-/Y}$ mice were as rare as for wild-type mice, indicating normal adaptation to the test situation (Fig. 7E and F, Table 1). Furthermore, *αPix/Arhgef6*$^{-/Y}$ mice made somewhat less serial choices than wild-type animals, indicating that their good performance was not due to increased use of stereotyped choice patterns (Table 1). These data indicate that *αPix/Arhgef6*$^{-/Y}$ mice can remember spatial information for at least several days, but have a strong tendency to perseverate on incorrect responses, resulting in inefficient navigation and slow adaptation to new targets.

αPix/Arhgef6$^{-/Y}$ mice show disinhibited object exploration

Exploratory and anxiety-related behaviors as well as locomotion were tested in the open field, elevated O-maze and emergence tests, which revealed normal levels and time course of locomotor activity and unaltered anxiety-related responses in *αPix/Arhgef6*$^{-/Y}$ mice (Supplementary Material, Fig. S12 and Table S1). When an unknown object was placed in a familiar arena, wild-type mice retracted to one of the corners, confirming their ability to perceive the object. They showed very little exploratory interaction with the object. In contrast, *αPix/Arhgef6*$^{-/Y}$ mice exhibited a striking increase in exploratory activity toward the object, spent little time in the corners, and were in closer contact with the object while exploring it (Fig. 7G and H and Table 1). Taken together, *αPix/Arhgef6*$^{-/Y}$ mice are normal with respect to activity and anxiety-related behavior in a novel environment, but overreact to changes in a familiar environment.

Complex positional learning in IntelliCage is impaired in *αPix/Arhgef6*$^{-/Y}$ mice

In many tests, mouse behavior is influenced by an interaction of handling stress and task requirements. Therefore, we tested mice in a familiar homecage set-up with their usual peers. Each mouse was marked by a subcutaneous microchip and was subjected individually to learning tasks in any of four corners providing opportunity for both spontaneous visits and operant conditioning by means of nose pokes and reward with water. During the adaptation period, both wild-type and *αPix/Arhgef6*$^{-/Y}$ mice showed similar numbers of visits and nose pokes (Fig. 8A). Similarly, no significant differences in visit activity were noticed when mice underwent a 24 h test for spatial preference learning (Fig. 8B). Both groups developed a significant preference for the correct corner (one sample *t*-test against chance level of 25%: control $t = 2.67$, $P < 0.05$; knockout $t = 3.84$, $P < 0.005$) (Fig. 8C). Thus, simple spatial preference learning was not altered in *αPix/Arhgef6*$^{-/Y}$ mice.

Upon exposure to a more complex combined place/position test with light signaling during drinking, *αPix/Arhgef6*$^{-/Y}$ mice significantly increased their visit activity during all 3 days of testing, making almost twice as many visits as wild-type animals ($P < 0.01$; Fig. 8D). Both groups made significantly more nose pokes into the correct openings than expected by chance (one sample *t*-test against 50% chance level: wild-type $t = 7.98$, $P < 0.001$; knockout $t = 6.52$, $P < 0.005$; Fig. 8E). Remarkably, the score of *αPix/Arhgef6*$^{-/Y}$ mice was significantly lower than that of wild-type animals ($P < 0.05$), indicating that the increased number of corner visits was associated with a higher error rate.

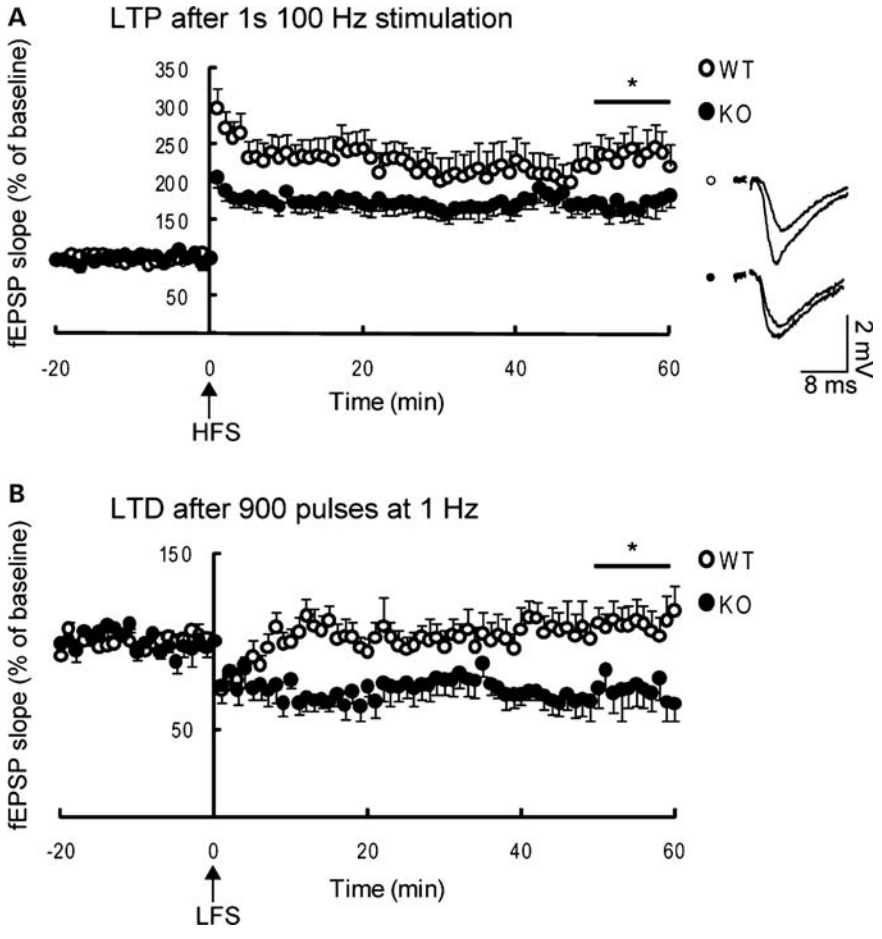

Figure 6. Altered synaptic plasticity in hippocampal area CA1 of *αPix/Arhgef6*$^{-/Y}$ mice. (**A**) E-LTP after high-frequency stimulation (100 Hz for 1 s) is decreased in *αPix/Arhgef6*$^{-/Y}$ mice. A significant decrease of ∼50% was found in *αPix/Arhgef6*$^{-/Y}$ animals over the last 10 min of recording (indicated by the asterisk; $P < 0.05$). Representative traces of fEPSPs from wild-type and knockout animals before and after HFS are shown on the right. $n = 8$ wild-type (WT) and 7 *αPix/Arhgef6*$^{-/Y}$ mice (KO). (**B**) LTD after low frequency stimulation (900 pulses at 1 Hz) was increased in *αPix/Arhgef6*$^{-/Y}$ mice. Whereas no LTD could be evoked in wild-type mice (WT), *αPix/Arhgef6*$^{-/Y}$ mice (KO) showed a significant depression of ∼30% over the last 10 min of recording (indicated by the asterisk; $P < 0.05$; $n = 7$). The level of 100% was defined as the mean fEPSP slope of the 20 baseline recordings before HFS or LFS at time 0 (arrow). Error bars represent SEM.

Further testing during 24 h with unpredictable reward from either the left or the right nose poke opening revealed that *αPix/Arhgef6*$^{-/Y}$ mice again made a significantly higher number of visits ($P < 0.05$; Fig. 8F). However, the percentage of correct responses was barely above the chance level in either group (Fig. 8G), in agreement with a task that was not solvable. Taken together, in *αPix/Arhgef6*$^{-/Y}$ mice, novel situations in the otherwise familiar home-cage environment induced increased activity that is associated with lower performance.

DISCUSSION

We report the functional characterization of a mouse mutant deficient for the X-linked ID gene *αPix/Arhgef6*. The behavioral and electrophysiological analyses indicated that *αPix/Arhgef6*$^{-/Y}$ mice exhibit specific deficits in behavior and cognition, such as impaired spatial and complex learning and excessive exploration of novel objects, as well as abnormalities in synaptic plasticity. This model allowed us to investigate the morphological and biochemical consequences of *αPix/Arhgef6* deficiency in mice. High levels of αPix/Arhgef6 in neuropil regions of the hippocampal formation suggest localization of αPix/Arhgef6 in dendritic and/or synaptic compartments. Overexpressed αPix/Arhgef6 was found to colocalize with PSD-95 in spine heads of excitatory synapses in cultured neurons (35), suggesting an important synaptic function of αPix/Arhgef6. Indeed, deletion of *αPix/Arhgef6* resulted in increased spine density and branching points on single neurons and, at the same time, in a total loss of spine synapses. Strong αPix/Arhgef6 expression in wild-type hippocampus along with reduced levels of active Rac1 and Cdc42 in the hippocampus of knockout animals suggest that altered activation of these Rho GTPases may underlie most, if not all, abnormalities observed in *αPix/Arhgef6*$^{-/Y}$ mice.

αPix/Arhgef6$^{-/Y}$ mice exhibit no obvious abnormalities in the gross anatomy of the CNS. Morphological analysis of the hippocampal CA1 region revealed changes in the global

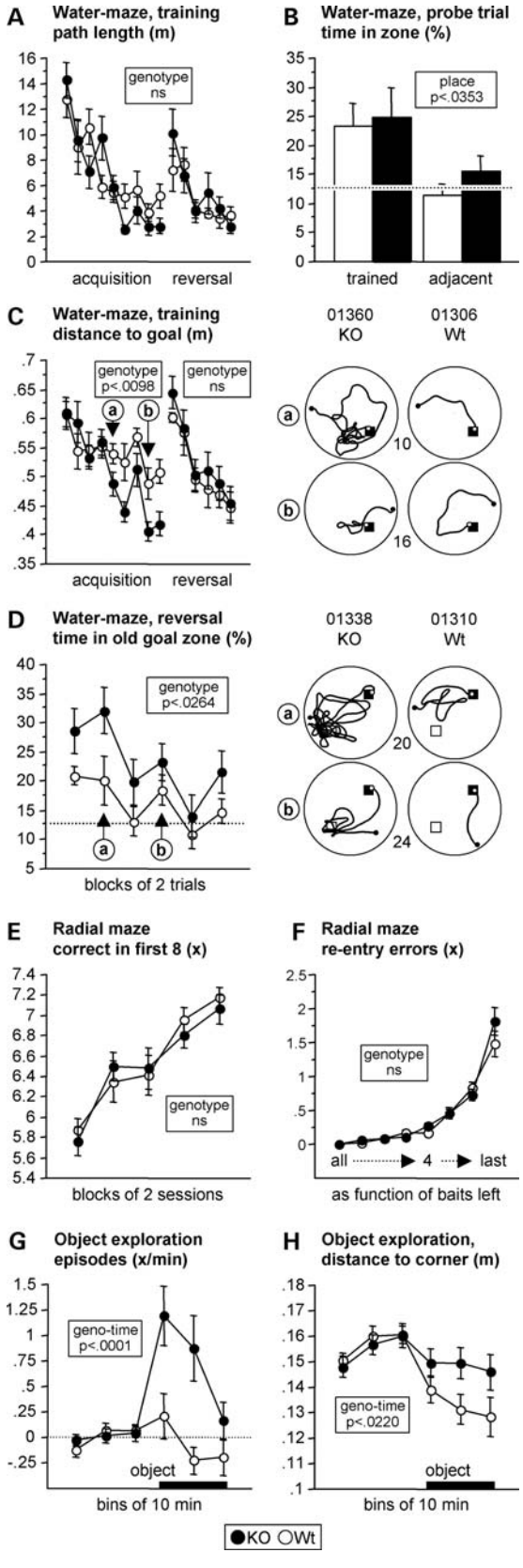

Figure 7. Distinct behavioral deficits in *αPix/Arhgef6*$^{-/Y}$ mice. Water-maze place navigation task (**A**–**D**), working memory procedure on the eight-arm radial maze (**E** and **F**), and object exploration (**G** and **H**). (A) Swim path length during place navigation acquisition and reversal. Each data point represents two consecutive trials. Performance and learning rate of *αPix/Arhgef6*$^{-/Y}$ mice were normal, with a trend toward slightly better performance during late acquisition [repeated analysis of variance (ANOVA): genotype ns (not significant), time $P < 0.0001$, interaction $P < 0.0612$; partial ANOVA time: KO $P < 0.0001$, Wt $P < 0.0001$]. *αPix/Arhgef6*$^{-/Y}$ mice tended to show a slightly larger performance drop after platform relocation (repeated ANOVA block 9–10: genotype ns, time $P < 0.0032$, interaction $P < 0.0710$). During reversal, escape performance of *αPix/Arhgef6*$^{-/Y}$ and wild-type mice recovered with similar efficiency (repeated ANOVA reversal: genotype ns, time $P < 0.0001$, interaction ns). (B) During the probe trial, both groups showed intact spatial preference for the trained goal zone, spending approximately twice as much of their time there than expected by chance (repeated ANOVA: genotype ns, place $P < 0.0353$, interaction place-genotype ns; one-sample *t*-test time in trained zone versus chance level of 12.5%: $P < 0.0179$). (C) Average distance to target (goal proximity) was reduced in *αPix/Arhgef6*$^{-/Y}$ mice, specifically during late acquisition (repeated ANOVA acquisition: genotype $P < 0.0098$, block $P < 0.0001$, interaction $P < 0.0458$; reversal: genotype ns, block $P < 0.0001$, interaction ns). Path plots of trials 10 and 16 of a representative *αPix/Arhgef6*$^{-/Y}$ and wild-type mouse are shown (a,b). (D) Amount of time spent in the old target zone during the first 30 s of all reversal trials (19–30) was strongly increased in *αPix/Arhgef6*$^{-/Y}$ mice. Each data point represents two consecutive trials (repeated ANOVA: genotype $P < 0.0264$, block $P < 0.0001$, interaction ns). Unlike wild-type mice, *αPix/Arhgef6*$^{-/Y}$ mice continued to show a significant preference for the old goal zone even during the second day of reversal training (one-sample *t*-test time in old goal zone versus chance level of 12.5% during trial blocks 10–12: $P < 0.0190$, KO $P < 0.0004$; trial blocks 13–15: Wt ns, KO $P < 0.0064$). Path plots of trials 20 (second reversal trial) and 24 (first trial of second reversal day) of a representative *αPix/Arhgef6*$^{-/Y}$ and wild-type mouse are shown (a, b). (E) *αPix/Arhgef6*$^{-/Y}$ mice showed normal performance and learning rate on the radial maze according to the number of correct responses in the first eight choices (repeated ANOVA: genotype ns, time $P < 0.0001$, interaction ns). (F) Independent of genotype, the average number of re-entry (working memory type) errors increased strongly with decreasing number of baits left on the maze (repeated ANOVA: genotype ns, baits $P < 0.0001$, interaction ns). (G) *αPix/Arhgef6*$^{-/Y}$ mice explored the novel object more often than wild-type mice (repeated ANOVA: genotype $P < 0.0051$, time $P < 0.0001$, interaction $P < 0.0001$) and showed strong exploratory activity toward the object, whereas object exploration was not significant in wild-type animals (partial ANOVA; KO: time $P < 0.0001$; Wt: time ns). (H) The decrease in the average distance to the nearest corner after introduction of the object was strongly attenuated in *αPix/Arhgef6*$^{-/Y}$ mice (repeated ANOVA: genotype ns, time $P < 0.0001$, interaction $P < 0.0220$; partial ANOVA time: KO $P < 0.0906$, Wt $P < 0.0001$).

dendrite structure as well as quantitative and qualitative alterations in spines of pyramidal cells in *αPix/Arhgef6*$^{-/Y}$ mice. These alterations include elongated apical and basal dendrites in 12-week-old *αPix/Arhgef6*$^{-/Y}$ mice, which are due to an increase in the number of branch points. Furthermore, an increase in the number of spines per dendrite was observed. In the mutant mice, we observed elongated spine necks, which have also been found in cultured rat hippocampal neurons when *αPix/Arhgef6* was knocked down (35). However, in contrast to our findings, a decrease in the ratio of mushroom-type spines versus filopodia and elongated spines has been identified in the same siRNA-treated hippocampal slice cultures (35). Similar discrepancies between *in vivo* and *in vitro* phenotypes have also been noted for other Rho-linked genes, such as *Ophn1* and *Pak3* (47–50). It has been proposed that the cellular environment may account for the distinct phenotypic effects as the environment of neurons and spines is much more complex *in vivo* compared with dissociated and slice cultures (49).

Table 1. Performance $\alpha Pix/Arhgef6^{-/Y}$ mice in behavioral tests of spatial learning and object exploration

	Genotype
Water-maze, acquisition training	
Escape latency (s)	↓ ns
Time in current goal quadrant (%)	↑ $P < 0.0054$ s 0.30
Average distance to goal (m)	↓ $P < 0.0097$ s 0.26
Wishaw's error (%)	↑ $P < 0.0280$ s 0.18
Cumulative chaining (x)	↓ ns
Time near wall (%)	ns
Swim speed (m/s)	↑ ns
Time floating (log s)	↓ ns
Path tortuosity (°/m)	ns
Circling index (°/m)	ns
Water-maze, probe trial	
Time in trained quadrant (%, chance 25%)	ns
Annulus crossing index (x/m)	ns
Water-maze, reversal training	
Escape latency (s)	ns
Time in current goal quadrant (%)	ns
Average distance to goal (m)	ns
Wishaw's error (%)	ns
Cumulative chaining (x)	ns
Time near wall (%)	↓ ns
Swim speed (m/s)	↑ ns
Time floating (log s)	ns
Path tortuosity (°/m)	↓ ns
Circling index (°/m)	↓ ns
Time in old goal quadrant (%, chance 25%)	↑ $P < 0.0457$ s 0.15
Annulus crossing index (x/m)	↑ $P < 0.0171$ s 0.22
Radial maze, working memory task	
Correct choices before 1st error (x)	↓ ns
Bait neglect errors (x)	↑ ns
Arm omission errors (x)	ns
Aborted choices (% of total)	↑ ns
Preferred choice angle (% of all angles)	↓ ns
Repeated angles (% of all angles)	↓ ns
Chaining (% of all angles)	↓ $P < 0.0335$ s 0.08
Visits to favorite arm (% chance)	ns
Object exploration	
Distance moved overall (m/min)	ns
Time in progressive locomotion (%)	ns
Time resting (%)	↓ ns
Velocity of progressive locomotion (m/s)	ns
Vertical movements overall (x/min)	↑ ns
Object exploration time (s/min)	↑ $P < 0.0157$ s 0.10
Object exploration episodes (x/min)	↑ $P < 0.0052$ s 0.14
Horizontal object exploration (m/min)	↑ $P < 0.0156$ s 0.10
Vertical object exploration (x/min)	↑ $P < 0.0124$ s 0.11
Distance to object while exploring (m)	↓ $P < 0.0103$ s 0.12

Factorial ANOVA was performed on measures that were averaged over the indicated observation periods. Type I error *P*-values are shown if <0.1, followed by estimated effect sizes as partial omega squared. Arrows indicate direction of mean differences if type 1 error $P < 0.25$. Conceptually related variables were grouped and significance levels adjusted starting from $P < 0.05$ using the false discovery ratio control procedure of Benjamini and Hochberg (90). s, significant; ns, not significant.

The lower number in spine synapses in $\alpha Pix/Arhgef6^{-/Y}$ mice suggest that there are more spines that do not participate in the formation of synapses in the hippocampi of $\alpha Pix/Arhgef6^{-/Y}$ mice as in wild-type mice. In *Ephrin-B3*$^{-/-}$ mice, fewer dendrite spines but normal numbers of synapses have been identified (51), suggesting that spine density and synapse density do not always correlate. Whether the observed changes in neuronal microstructure in $\alpha Pix/Arhgef6^{-/Y}$ mice are the primary cause or merely a downstream consequence of the spine synapse loss is an open question at present. We put forward two hypotheses to explain these findings. First, deletion of *αPix/Arhgef6* may lead to an overall loss in spine synapses in the hippocampus of adult knockout animals. As a compensatory mechanism intact pyramidal neurons extend new dendritic branches and protrusions which do not necessarily form spine synapses. Secondly, deficiency of αPix/Arhgef6 may cause developmental changes in neuronal fine structure, such as overabundance of dendritic spines and enhancement of dendritic branching. Such megadendrites have also been described in patients with severe ID (16) and in dentate gyrus granule cells with conditional deletion of the *Pten* gene, in which mutations can lead to macrocephaly and autism spectrum disorders in humans (52,53). An increase in the dendritic field of a neuron is consistent with an enlargement of its receptive field so that it receives greater convergent inputs than less densely branched neurons (54). Such an overextended network may give rise to overconnectivity and neuronal overexcitability resulting in synapse loss in hippocampal area CA1 of $\alpha Pix/Arhgef6^{-/Y}$ mice. As spine synapse loss in $\alpha Pix/Arhgef6^{-/Y}$ mice started at age 10 weeks, while altered dendritic morphology was already found in 8-week-old mice, the latter hypothesis seems more likely.

Behavioral characterization of *αPix/Arhgef6*-deficient mice revealed largely intact performance in basic tests of spatial reference and working memory, as well as normal day-to-day habituation to a novel arena. However, more complex spatial learning and flexibility was impaired in $\alpha Pix/Arhgef6^{-/Y}$ mice. In the water maze, mutant mice produced small navigation errors and showed spatial perseverance when they had to adapt to a changed goal position. In IntelliCage testing, when spatial complexity was increased, we observed significantly increased visit activity associated with more left/right choice errors in the mutant mice. Exaggerated increases in activity were also observed when mutant mice were confronted with an unsolvable task in IntelliCage or when an unknown object was introduced in a familiar environment. Taken together, these observations suggest deficient behavioral control and altered processing of complex spatial information in $\alpha Pix/Arhgef6^{-/Y}$ mice. Two other mouse models for X-linked ID, *Rsk2* and *Ophn1* null mice, are impaired in spatial learning and exhibited alterations in exploratory behavior (49,55), similar to $\alpha Pix/Arhgef6^{-/Y}$ mice. Thus, learning deficits in combination with hyperreactivity in exploration tests may represent common behavioral changes in mouse models mimicking the human ID phenotype. Taken together, $\alpha Pix/Arhgef6^{-/Y}$ mice are able to cope well with simple learning tasks; however, they show problems in complex spatial learning, associated with deficits in coping with altered learning situations or sensory stimuli. These data indicate a decreased behavioral control of $\alpha Pix/Arhgef6^{-/Y}$ mice in more demanding or mildly stressful situations. In this sense, their behavior resembles, at least in part, that of individuals with the fragile X syndrome, another form of X-linked ID (56–58).

Our biochemical analysis revealed that levels of the active form of Rac1 and Cdc42 were significantly reduced in the

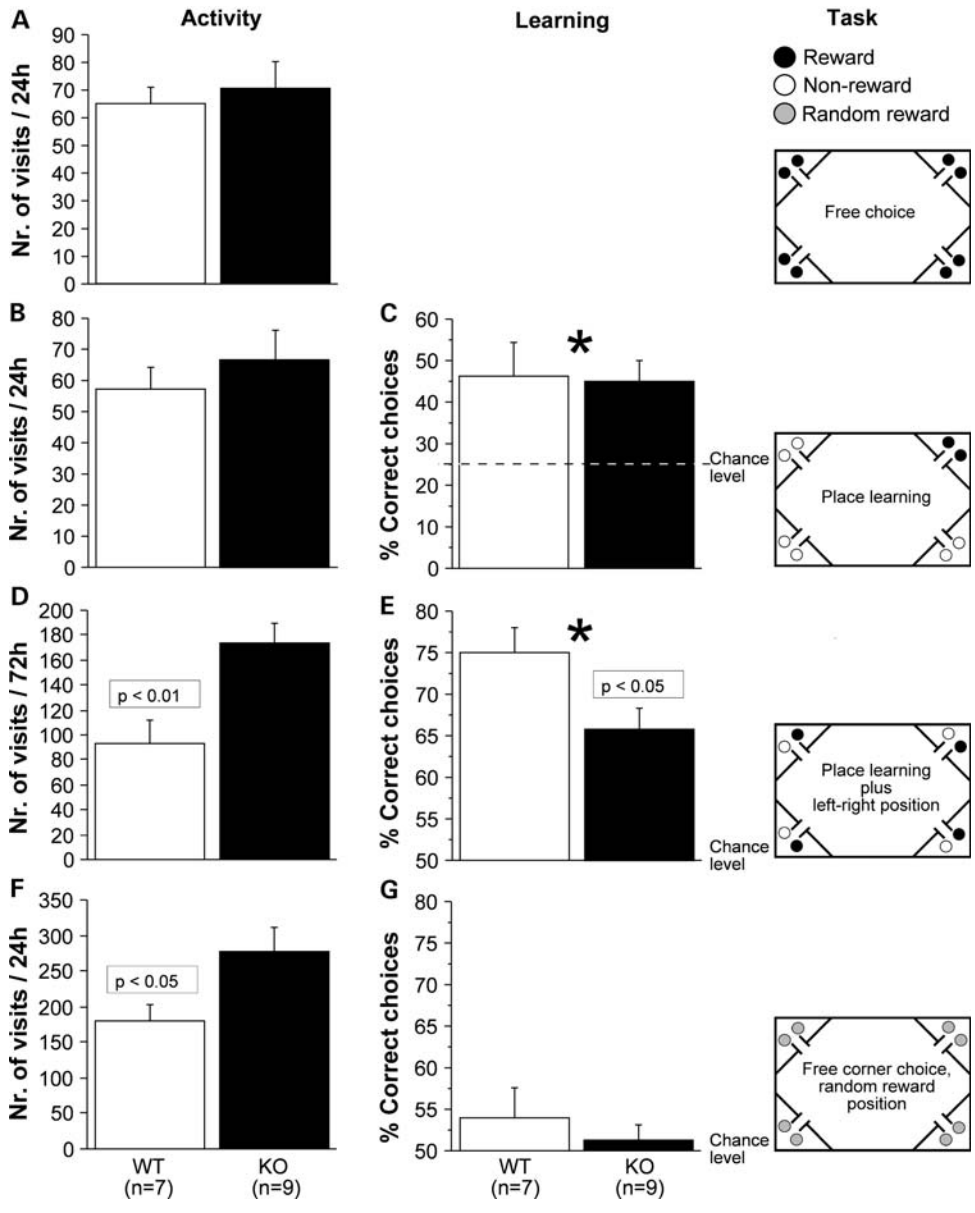

Figure 8. Changes in complex positional learning of *αPix/Arhgef6*$^{-/Y}$ mice in IntelliCage^{TM}. The left column (diagrams **A**, **B**, **D**, **F**) indicates activity levels as expressed by the average number of visits (and SEM) to corners during a defined period. Middle column (diagrams **C**, **E**, **G**): averaged learning scores (percentages of correct responses and SEM) in solvable and non-solvable positional learning paradigms. Right-hand column depicts tasks to which the mice were subjected. (A) No significant difference in the number of corner visits during 24 h of adaptation to IntelliCage. (B) No significant difference in visit activity during a simple place learning task. (C) Both *αPix/Arhgef6*$^{-/Y}$ and wild-type mice developed an equal corner preference in simple spatial learning. (D) Introducing a complex positional learning paradigm entailed a significant increase in corner visits in *αPix/Arhgef6*$^{-/Y}$ mice. (E) Despite of more visits, *αPix/Arhgef6*$^{-/Y}$ mice committed significantly more choice errors in a complex positional learning paradigm. (F) In face of an unsolvable positional paradigm, *αPix/Arhgef6*$^{-/Y}$ mice showed again significantly increased visit activity. (G) Chance level performance of both *αPix/Arhgef6*$^{-/Y}$ and wild-type mice in a task presenting randomly changing positions of reward indicated that the concomitant (but not preceding) illumination (green for a correct choice; red for a wrong nose poke) did not play a role in learning of the complex positional task before. *Significant learning effects in both groups of mice as tested against expected chance levels.

hippocampus and unchanged in the cerebral cortex and cerebellum of adult *αPix/Arhgef6*$^{-/Y}$ mice. This correlates well with the rather high abundance of αPix/Arhgef6 in the hippocampus; other Rho GEFs are likely to be more relevant for GTPase activation in the cortex. Our data suggest that αPix/Arhgef6 deficiency affects the activity state of these two GTPases in the brain, although protein levels and/or activation of several cytoskeletal regulators were only slightly affected. As the GEF activity of αPix/Arhgef6 towards Cdc42 and Rac1 has been repeatedly demonstrated by *in vitro* assays (27,29,31,34), a direct influence of αPix/Arhgef6 loss on Rac1 and Cdc42 activation in the knockout mouse is likely, particularly because the activity state of RhoA was not altered. However, we cannot yet exclude a rather indirect

effect on activation of Rac1 and Cdc42 upon αPix/Arhgef6 deficiency. Together, we suggest that changes in brain microstructure, deficits in learning and memory as well as altered synaptic plasticity could be collectively caused by deregulated activity of Rac1 and Cdc42 in the hippocampus of mutant animals. Indeed, pharmacological inhibition of Rac activity has been shown to reduce LTP (59), while activation of Rac1 resulted in enhanced LTP induction and improved hippocampus-dependent learning (60). Therefore, deficits in E-LTP and various forms of hippocampus-dependent learning in *αPix/Arhgef6*$^{-/Y}$ mice could be due to a failure in fine-tuning of Rac1 activity. Stimulus-dependent impairments in long-term synaptic plasticity have also been observed in *Il1rapl1*-deficient mice, another mouse model of X-linked ID. These deficits were associated with a reduction in both dendritic spine density and excitatory synapses in the CA1 region of the hippocampus, suggesting an involvement of Il1rapl1 in promoting the formation or stabilization of excitatory synapses (61). Similarly, the Rho-linked protein Ophn1 and its Rho-GAP activity have been implicated in controlling synapse maturation and synaptic plasticity by stabilizing AMPA receptors at the synapse (62).

Collective data indicate that the balance between RhoA, Rac1 and Cdc42 activities determines dendritic and spine morphology via regulation of the actin cytoskeleton. While active Rac1/Cdc42 stimulates dendritic growth and branching as well as spine formation and maintenance, active RhoA negatively regulates these processes (5). We, however, observed reduced Rac1 and Cdc42 activity along with an increased density of spines and elongated apical and basal dendrites in *αPix/Arhgef6*$^{-/Y}$ mice suggesting that cytoskeletal dysregulation may not underlie the defects in our mouse model. Besides their role in actin dynamics, Rho GTPases are also implicated in membrane dynamics and vesicle trafficking (63), and it has been demonstrated that the Rho and Rac pathways modulate receptor endocytosis (64,65). In line with this, the RhoGAP Ophn1 exerts a potent stimulatory effect on synaptic vesicle and AMPA receptor endocytosis by binding to endocytic proteins (66,67). Similarly, the αPix homologue βPIX interacts with the E3 ubiquitin ligase Cbl (68), a molecule crucially involved in vesicular trafficking of the epidermal growth factor (EGF) receptor (69). βPIX binding to Cbl prevents EGF receptor internalization and subsequent downregulation (70,71). Interestingly, αPIX also interacts with Cbl proteins (68, Rosenberger, unpublished data). We speculate that αPix/Arhgef6 could regulate vesicular trafficking in a way similar to βPIX and endocytic and/or trafficking defects may underlie altered neuronal connectivity and impaired synaptic function and cognition in *αPix/Arhgef6*$^{-/Y}$ mice.

In summary, our data provide evidence that αPix/Arhgef6 is essential for cognitive function and synaptic plasticity, such as Ophn1 and Pak3, all of which are involved in Rho GTPase signaling (10,49,50,72). Importantly, αPix/Arhgef6 does not only have a crucial function in the nervous system, as it is also required for lymphocyte development and immune functions (73). Therefore, uncovering the pathophysiological mechanism underlying the abnormalities in *αPix/Arhgef6*$^{-/Y}$ mice will be extremely useful in gaining a better understanding of disorders affecting both the immune and neuronal system.

MATERIALS AND METHODS

Generation of *αPix/Arhgef6* knockout mice

Cosmid MPMGc121K04251Q was isolated from the 129/ola genomic library and provided by the RZPD Deutsches Ressourcenzentrum für Genomforschung GmbH, Berlin, Germany. We confirmed the presence of *αPix/Arhgef6* exons 1 and 2 by STS typing and sequencing. A targeting vector was constructed by inserting a neomycin resistance cassette in exon 1 of *αPix/Arhgef6* (Fig. 1A). The vector was designed to eliminate 246 bp of *αPix/Arhgef6* coding region of exons 1 and 2 as well as adjacent sequences comprising intron 1 and part of intron 2. We used the embryonic stem (ES) cell line R1, an ES cell line of mixed genetic background of mouse strain 129 (129X1 × 129S1)F1, for targeting the *Arhgef6* locus. G418-resistant R1 ES clones were initially analyzed for a homologous targeting event by multiplex PCR using primers knockout-in (5′-ACTGTCACTGTGAGATTGTCTGAGGA C-3′), M_GEF7 (5′-TTGCACAACACTACCCCATTTTT CAGC-3′) and tau1 (5′-GCATGATCTTCCATCACGTCGAA CTCC-3′). PCR-positive clones were confirmed by Southern blotting using a 5′ external probe, SB3, a genomic amplicon of 590 bp from primers 152AP1 (5′-CTATTA CATAGATTTGGCCATGGCTC-3′) and 152AP6 (5′-GTGC TATTACTGGTGGTCACAATCTG-3′). Southern blots were done by standard methods. Three positive ES cell clones were injected into C57BL/6 blastocysts, which were then transferred into pseudopregnant female recipients. The resulting chimeric mice were crossed to C57BL/6 mice to generate an N1 population. *αPix/Arhgef6*$^{-/Y}$ mice derived from three independent targeted ES cell lines were phenotypically indistinguishable. Genotypes of all animals were determined by PCR from tail DNA using primers knockout-in and tau1 resulting in a 695 bp product from the knockout allele and primers knockout-in and M_GEF7 which yielded a 785 bp fragment from the wild-type allele.

Protein isolation from mouse tissues and western blotting

Tissues from adult wild-type and *αPix/Arhgef6*$^{-/Y}$ mice were dissected, immediately placed on dry ice and homogenized by grinding frozen tissue in ice-cold lysis buffer [140 mM NaCl; 20 mM Tris–HCl, pH 7.6; 5% glycine; 1% NP-40; 0.1% SDS, 1 tablet Complete^{TM} Mini protein inhibitor cocktail (Roche)/30 ml; 0.5 mg/ml pefablock (Roche)]. The homogenates were cleared by three centrifugation steps at 14 000*g* for 10 min. Samples were subjected to GTPase activation assays or sodium dodecyl sulfate polyacrylamide gel electrophoresis (SDS–PAGE) followed by immunoblotting using monoclonal rabbit anti-human αPix/Arhgef6 antibody (Cell Signaling Technology, Danvers, MA, USA; no. 4573; 1:1000 dilution).

Immunohistochemistry

Adult *αPix/Arhgef6*$^{-/Y}$ and wild-type mice (73) were deeply anesthetized using isoflurane and decapitated. Brains were removed and frozen on an aluminum block cooled by liquid nitrogen. Twenty-five micrometer sagittal sections were cut using a cryostat and mounted on slides. Dried sections were treated

with acetone for 10 s at room temperature, fixed in a solution of 4% formaldehyde in 0.1 phosphate buffer pH 7.4 for 20 min at 4°C and subsequently used for immunohistochemistry. Sections were washed three times in phosphate-buffered saline (PBS, pH 7.4) and incubated in a solution containing 10% normal donkey serum and 0.3% Triton X-100 for 60 min followed by the rabbit monoclonal anti-αPix antibody (Cell Signaling Technology; 1:100 dilution) in the same solution supplemented with 0.1% sodium azide over night at room temperature. After washing in PBS and incubation in PBS containing 0.1% Triton X-100 and 0.2% bovine serum albumin (PBS-A, 60 min), the sections were incubated with the Cy3-labeled anti-rabbit antibody (Dianova; 1:2000 dilution) in PBS-A for 4 h at room temperature and mounted in DABCO/Mowiol. Analysis was performed with an AxioImager microscope (Zeiss). Images were taken using a microscope camera AxioCam MRC and the Axiovision software 4.7 (Zeiss) and imported into Adobe Photoshop7.0 to mount composite displays.

GTPase activation assay

GST-PAK[PBD] and GST-Rhotekin[RBD] fusion proteins were isolated from *Escherichia coli* strain BL21 transformed with pGEX-2TK-PAK[PBD] and pGEX-2TK-Rhotekin[RBD], respectively, by snap freezing in liquid nitrogen and sonification. Subsequently, fusion proteins were coupled with glutathione-bound agarose beads (Novagen), washed in wash buffer (50 mM Tris–HCl, pH 8.0; 50 mM NaCl; 5 mM $MgCl_2$) and finally diluted to 50% slurry with wash buffer. Cortices, cerebelli and hippocampi of 3-month-old mice were lysed as described above. Hippocampi of two mice each were pooled to obtain sufficient protein for GTPases activation assays. After withdrawal of samples to assess total GTPase levels, equal amounts of protein lysates were incubated with 20 μg of the GST-fusion protein solution for 45 min at 4°C to trap the active forms of Rac and Cdc42 or Rho. Beads were precipitated by centrifugation at 500*g* and washed in lysis buffer. Total cell lysates and precipitates were separated by SDS–PAGE and GTPases were detected using mouse monoclonal anti-Cdc42 (clone 44, 1:1000 dilution; BD Transduction Laboratories, Heidelberg, Germany), mouse monoclonal anti-Rac (clone 23A8, 1:1000 dilution; Millipore, Schwalbach, Germany) and mouse monoclonal anti-RhoA (clone 26C4, 1:400 dilution; Santa Cruz Biotechnology, Heidelberg, Germany) antibodies.

Golgi-Cox impregnation

Brains of 12-week-old adult *αPix/Arhgef6*$^{-/Y}$ mice ($n = 5$) and wild-type littermates ($n = 4$) and of 8-week-old *αPix/Arhgef6*$^{-/Y}$ mice ($n = 2$) and wild-type littermates ($n = 8$) were immersed for 21 days in Golgi-Cox solution (1% potassium dichromate; 1% mercuric chloride; 0.8% potassium chromate in Milli-Q water) (74). Subsequently, the brains were rinsed four times in Milli-Q water, dehydrated by consecutive incubations in 70, 96 and 100% EtOH and embedded in celloidin by successive incubations in 3, 6 and 12% celloidin. Celloidin was cleared with chloroform before 200 μm coronal sections were cut using a sledge-microtome. After every fifth section, two 50 μm sections were cut for Nissl staining. The Golgi-Cox staining was developed by incubation in 16% ammonia for 30 min and subsequent fixation in 1% sodium thiosulphate for 7 min. The 50 μm sections were counterstained with 0.5% cresylviolet. Sections were dehydrated by successive incubations in 70 and 96% EtOH and 100% butanol, cleared in Histo-clear (Biozym, Landgraaf, The Netherlands) and embedded in Histomount (National Diagnostics, Atlanta, Georgia, USA).

Dendritic reconstruction of Golgi impregnated sections

All object slides were coded to assure unbiased recording and reconstruction of the neurons. Decoding was performed during statistical analysis. Neurons were recorded from the middle of the sections in 3D image stacks (99 focal planes with 1 μm spacing) with the program Image-Pro Plus, version 5.1.1.38 (Media Cybernetics, Silver Spring, MD, USA) using an Axioplan2 microscope (Zeiss) with a ×40 air objective (Plan-apochromat, Zeiss) and a digital black and white EvolutionQEi camera (Media Cybernetics). For this purpose, neurons were used in which the apical dendrite was parallel to the cutting plane. Pyramidal neurons were randomly selected at low magnification, where spines were hardly visible. About 10 randomly selected neurons per animal were recorded and manually reconstructed with the ImagePro Plus 5 application Neurodraw (developed by K. de Vos, J. van Heerikhuize and C.W. Pool, Netherlands Institute for Neuroscience, Amsterdam, The Netherlands). This program stores the three-dimensional coordinates of all structures of the neuron as well as the type of structure (soma outline, apical or basal dendrite, branch points, filopodia or spines etc.). Branch points were defined as locations where dendrites or dendritic segments split into two or occasionally three distal segments. Upon reconstruction, the Neurodraw program calculated the following parameters: surface area of the soma, number of dendrites per cell and for both apical and basal dendrites: total dendrite length, number of branch points, terminal segment length and intermediate segment length. Statistical analysis was performed with SPSS 12.0.1 (SPSS Inc., Chicago, IL, USA). Since most parameters were not normally distributed, the non-parametric Mann–Whitney *U* test was used to test for significance.

Spine counts

Per animal, dendritic spine density of 10 pyramidal neurons in hippocampus CA1 area was quantified using the same Golgi-Cox impregnated sections as were used for the dendritic reconstructions. Spines were counted all along the apical dendrite (including the side-branches) in consecutive 20 μm stretches and in a single 10 μm stretch at 50 μm from the soma on basal dendrites. A total number of 1683 protrusions on apical dendrites from 15 neurons of four wild-type and four *αPix/Arhgef6* knockout mice were analyzed. A random subset of spines along the apical dendrites between 190 and 210 μm from the soma was analyzed for three spine morphology properties: spine head size, spine (neck) length and spine neck width.

Protrusions were classified as spines if they contained a terminal thickening (a head) or as filopodia if they did not contain a distinct head. The non-parametric Mann–Whitney test was used to test for statistical significance in SPSS 12.0.1.

Cortex and hippocampus volume measurement

Nissl-stained brain sections were recorded using the Capture Image program in Image Pro Plus 4.5 software (Media Cybernetics). Images were recorded with a ×2.5 plan-neofluor objective (Zeiss) using an Axioskop microscope (Zeiss) equipped with a color video camera (JVC). The cerebral cortex and the hippocampus were outlined and the area was measured in 7–10 sections with equal spacing, the first section being chosen randomly, using the Carmilla application of Image Pro Plus (developed J. van Heerikhuize and C.W. Pool, Netherlands Institute for Neuroscience, Amsterdam, The Netherlands). Total cortex and hippocampus volume for each animal was then calculated by summation of the cortex or hippocampus areas of all sections measured per animal, multiplied by the distance between the sections [the Cavalieri method (75,76)].

Cell counts in hippocampus CA1 pyramidal layer by optical dissector method

Four adult *αPix/Arhgef6* knockout mice and five wild-type littermates (all 16 weeks old) were deeply anaesthetized with 0.1 ml/g bodyweight ip Nembutal (Ceva Sante Animale B.V., Maassluis, The Netherlands) and perfused via the left cardiac ventricle with PBS containing 50 IE heparin, followed by 4% paraformaldehyde in PBS. Brains were postfixed in 4% paraformaldehyde in PBS for three nights at 4°C. Right hemispheres were dehydrated, embedded in celloidin and sectioned at 50 μm in the coronal plane using a sledge-microtome. Sections were stained with 0.5% cresylviolet, dehydrated, cleared in xylene and embedded in Enthallan (Merck, Darmstadt, Germany).

Every fifth section of 50 μm was selected for cell counting in pyramidal layer of hippocampus CA1 area after choosing the first section randomly. In the ImagePro Plus 5 application Cell Count, the CA1 pyramidal layer was outlined at low magnification using an Axioskop microscope (Zeiss) and a systematic random selection was made of the areas in which cells would be counted at high magnification. In these areas, the neuronal cell bodies, which came into focus within the 10 μm high optical dissector, were counted manually using a 63× oil immersion lens (Zeiss). By counting neurons in sections throughout the whole CA1 pyramidal layer, the total number of neurons in this structure could be calculated (77).

Definition of hippocampus CA1 area in Nissl-stained sections

The border between CA1 and subiculum was defined by the area where the somata became smaller and the cytoplasm was more intensely stained. The border of CA1 to CA2 was defined by the area where the somata in the pyramidal layer started to become bigger than those in CA1. The cytoplasm of the somata in CA2 was somewhat less stained compared with CA1, cells were less aligned and somewhat less densely packed.

Electron microscopy and calculation of spine synapse density

Small hippocampal tissue blocks were postfixed in 1% osmium tetroxide for 30 min, dehydrated in graded ethanol using 1% uranyl acetate in 70% ethanol for 30 min and embedded in epoxy resin. After capsule embedding, blocks were trimmed to contain only the stratum pyramidale and stratum radiatum up to its transition to stratum lacunosum-moleculare of the CA1 hippocampal subfield. To avoid bias, the tissue samples were coded so that the investigator was not aware of the genotype of the analyzed material.

To determine spine synapse density, we used unbiased stereological methods as previously described (78). Briefly, pairs of consecutive serial ultrathin sections of a defined thickness (0.09 μm) were cut and collected on formvar-coated single grids. The sections contained either the upper or the middle third of the CA1 stratum radiatum of the hippocampus where projections from the CA3 region predominantly terminate (79). Electron micrographs were made from pairs of consecutive sections at a magnification of ×6600. Areas occupied by interfering structures, such as large dendrites or blood vessels, were intentionally avoided. To obtain a comparable measure of synaptic numbers, unbiased for possible changes in synaptic size, the dissector technique was used (80). The density of spine synapses of pyramidal cell dendrites was calculated with the help of a reference grid superimposed on the EM prints. Only those spine synapses were counted that were present on the reference section but not on the look-up section. Spine synapses were defined by a presynaptic bouton, which contained presynaptic vesicles, and by a synaptic spine, which exhibited a PSD. The dissector volume was calculated by multiplying the unit area of the reference by the distance (0.09 μm) between the reference and the look-up section (81). At least 20 neuropil fields per tissue sample and animal were analyzed and the mean was calculated for each animal. For statistical analysis, these means were compared between the two groups. Thus, tests for normality and equal variance were followed by a two-tailed *t*-test. *P*-values <0.05 were considered to be significant.

Long-term plasticity in hippocampus CA1 area

Long-term plasticity was recorded in *αPix/Arhgef6* knockout mice and wild-type littermates at the age of 10–14 weeks. Eight wild-type and seven *αPix/Arhgef6* knockout mice were used for LTP and seven wild-type and seven *αPix/Arhgef6* knockout mice were analyzed for LTD. Hippocampal slices of 400 μm thickness were prepared after decapitation and kept in ACSF (120 mM NaCl; 3.5 mM KCl; 1.3 mM $MgSO_4 \cdot 7H_2O$; 1.25 mM NaH_2PO_4; 2.5 mM $CaCl_2 \cdot 2H_2O$; 10 mM glucose; 25 mM $NaHCO_3$, gassed with 95% O_2 and 5% CO_2) for 1 h at room temperature before being transferred to the holding chamber. During measurements, slices were constantly perfused with oxygenated ACSF at 31.5°C. The stimulation electrode (bipolar, stainless steel) was placed on the Schaffer collaterals in the CA1 region. A low-resistance glass microelectrode (filled with ACSF) was used to record the field potentials (fEPSP) from stratum radiatum of CA1. Before starting each experiment, an input/output curve was made by gradually increasing stimulation intensity starting from no response until the maximum response amplitude was reached. The stimulation intensity that evoked half maximal fEPSP amplitude (I_h) was used for 20 min of baseline recording, stimulating once every 60 s. LTP was evoked by

high-frequency stimulation (1 s at 100 Hz). LTD was evoked by low-frequency stimulation (900 pulses at 1 Hz). After stimulation, the response was monitored for 1 h, again with one stimulus every 60 s.

Preparation of PSD

PSD was prepared from mouse forebrain according to the method of Carlin *et al*. (82). Briefly, a membrane fraction obtained by centrifugation (14.000*g*; 15 min; 4°C) of postnuclear supernatants was further fractionated by sucrose density gradient centrifugation (82 500*g*). The synaptosomal fraction, which recovered at the interface between 1.0 and 1.2 M sucrose, was extracted with 0.5% Triton X-100, and the PSD fraction was subsequently isolated by centrifugation at 32 800*g*.

General procedures and animals for behavioral analysis

Animals for standard behavioral tests. Both standard behavioral tests and IntelliCage experiments were approved by the Veterinary office of the Canton of Zurich. The mice were transferred to single cages before the beginning of the experimental period and examined during the dark phase of the cycle. Two cohorts of male mice were tested as follows. A first cohort did all tests (12 knockouts and 9 wild-types, 18–27 weeks at begin of testing): water maze, radial maze, open field, O-maze, emergence test and object exploration. One wild-type and one knockout mouse yielded no usable probe trial data in the water maze because they accidentally hit the new platform immediately after release. A second cohort (13 knockouts and 14 wild-types, 31–46 weeks at begin of testing) was used to replicate the radial maze, emergence and object exploration tests. All experiments were video-tracked using a Noldus EthoVision 1.96/2.30/3.00 system (Noldus Information Technology, Wageningen, The Netherlands) and raw data were transferred to the program Wintrack (83) (www.dpwolfer.ch/wintrack) for analysis.

Animals for IntelliCage^{TM} *test*. Sixteen male mice (seven wild-types and nine *αPix/Arhgef6* knockout mice) of an average age of 6 months were used for these experiments. They consisted of two groups of mixed genotypes that had been housed together since weaning. One group included four mutants and four wild-types, the other group included five mutants and four wild-types. One week before the experiment, they were anesthetized by inhalation of isoflurane vapor and subcutaneously injected with glass-covered microtransponders (11.5 mm length, 2.2 mm diameter; Trovan, ID-100) and returned to their cages for 48 h. This passive transponder emits a unique animal identification code when activated by a magnetic field. All animals recovered from the anesthetic within minutes of exposure and were later checked with a handheld scanner for retention of transponders before introduction to the IntelliCages.

Behavioral procedures

Maze learning and exploration tests. Place navigation in the water maze was tested as described previously (84). In brief, a white circular pool (150 cm diameter) contained milky water (24–26°C). Acquisition training consisted of 18 trials (6 per day, inter-trial interval 30–60 min) during which the submerged platform (14 × 14 cm) was left in the same position. Trials lasted a maximum of 120 s. To monitor reversal learning, the platform was moved to the opposite position for two additional days of training (six trials per day). The first 30 s of the first reversal trial served as probe trial to test for spatial retention.

The working memory procedure on the 8-arm radial maze was carried out as described previously (85). Briefly, mice were reduced to and maintained at 85% of their free-feeding body weight. After two habituation sessions, the mice were trained for 10 days with one trial per day during which they could move freely on the maze for maximum 10 min to collect a total of eight cereal pellets from the ends of the maze arms (7 × 38 cm, clear Perspex side walls).

Exploratory activity and anxiety-related responses were tested as described previously (86). In brief, the object exploration test began on the day following the 30 min emergence test (87) with the mice habituating to the same square arena (50 × 50 cm) for further 30 min, but without home box. Then, a 50 ml Falcon tube was placed vertically into the center of the arena and observation continued for another 30 min. The arena was divided into an object zone from which the animal could at least touch the object (18 cm diameter, 10% of surface), a wall zone (36% of surface, 5 cm wide) and a transition zone in between. All zone definitions were based on average occupancy by a large population of mice. In each zone, recorded tracks were segmented into three motion states according to criteria modified from reference (88): bouts of progressive locomotion, episodes of small lingering, movements which correlated with various exploratory behaviors such as rearing and resting phases (also including grooming). Vertical activity was estimated from changes of apparent subject area in the absence of progressive locomotion.

IntelliCage^{TM} *test*. IntelliCage^{TM} is an automated learning apparatus assessing spontaneous and learning behavior of group-caged mice (NewBehavior AG, Zürich, Switzerland). The system fits into a large standard rat cage (Techniplast 2000) measuring 55 × 37.5 cm at the base, 58 × 40 cm at the top, with a height of 20.5 cm. A cover plate holds four operant learning chambers that fit into the corners of the housing cage, covering a triangular 15 cm × 15 cm × 21 cm area of floor space each. Access into the chamber is provided via a tubular antenna reading the transponder codes (50 mm outer and 30 mm inner diameter). This design restricts access to the learning chamber to one mouse. The chamber, equipped with a proximity sensor, contains two openings of 13 mm diameter permitting access to the nipples of drinking bottles. These openings are crossed by photobeams recording nose pokes of the mice. Access to the tubes can be barred by small motorized doors. In addition, each cage contained a sleeping shelter in the center on which the animals could climb to reach the food (*ad libitum*). The two IntelliCages were controlled by a microcomputer recognizing visits, nose pokes and tube lickings of individual mice, and delivering reward (by opening the access to water after a nose poke) or punishment (by entering the test chamber) according to the

preprogrammed schedules. The cages were located in a room of the animal facilities. The system ran continually for many days, behavioral activity of the mice being monitored from the experimenter office via Intranet.

Test protocols for adaptation, spatial and discrimination learning. The mice spent 2 weeks in the IntelliCages, during this time they underwent several test protocols. During the first 24 h, the system assessed adaptation to the new situation by measuring how frequently the mice entered the tubes to the corners and the number of nose pokes into the openings with all doors open. During the next 24 h, a place preference test was conducted. Each mouse was assigned to one of the four corners, two to three mice sharing the same assignment. Upon entering a non-assigned corner, the openings to the drinking nipples remained barred after nose pokes. In the correct corner, a nose poke into either the left or the right opening would trigger opening of the barring gates and the mouse was allowed to drink without time limits. In order to make the spatial learning more difficult, a test combining spatial and positional features was run for 3 days. Each mouse could enter any corner, but in two of the corners, the correct opening was always located at the left side, while it was on the right side in the two other corners (see also Fig. 8, third column). For performing a correct nose poke, the animals had thus to remember the correct left/right position of the opening for the corners. In order to allow for this type of learning, the nose poke switched on three LED above the opening, green when the mouse was poking the correct hole and red when it was poking the wrong side. These colors can be discriminated by mice (H.-P. Lipp, unpublished data), yet presumably because of the different luminosity of the light sources. Variables presented here are the number of visits (a measure of basic activity) and the percentage of correct nose pokes. This test was followed by 24 h of testing the animals for their behavior in a non-solvable task. The mice could again enter all corners freely, but the correct side for the first nose poke varied randomly between left and right. As in the task before, performing a nose poke switched on green lights on the correct side, and red lights on the wrong side. The animal was allowed additional nose pokes after a choice, but the correct side altered unpredictably. Variables measured were the number of visits and the percentage of 'correct' nose pokes (expected to be at chance levels, 50%).

Statistics

Behavioral data were analyzed using a one-way factorial analysis of variance (ANOVA) model with genotype (knockout, wild-type) as between subject factor. Floating time in the water maze and latency measures in the exploration tests were log transformed. Where applicable, we added cohort as second between subject factor in order to reduce unexplained variance and to check for cohort dependence of genotype effects. Because none of the genotype effects was cohort dependent, the cohort factor is not reported in the figures and tables. As needed to analyze time and zone dependence of effects, the ANOVA model was expanded by inclusion of within subject factors trial (block) or zone as indicated in the figure legends. Effects were considered significant if $P < 0.05$, non-significant trends are reported up to $P < 0.10$. Effect sizes were estimated as partial omega squared (89), the proportion of variance accounted for by genotype if only the factor of interest were in the design, range 0–1.0. One sample *t*-tests were used to compare group means with hypothesized means such as chance values. Statview 5.0.1 (no longer commercially available) or MS Excel 2003 was used for all statistical computations.

SUPPLEMENTARY MATERIAL

Supplementary Material is available at *HMG* online.

ACKNOWLEDGEMENTS

We thank Tina Koppelmann for technical assistance with ES cell culture and generation of chimeric mice, Inka Jantke and Ellen Kampert for genotyping of mice, Nikos Green and Carlyn Mamber for morphological analyses, Inger Drescher for expert help with behavioral testing, and Behnam Nissan for taking care of animals.

Conflict of Interest statement. None declared.

FUNDING

This work was supported by the Deutsche Forschungsgemeinschaft (FOR885/IRP5 to K.K. and G.R., FOR885/IRP2 to H.-J.K. and SFB854/TP11 to K.D.F.); the European Commission (QLG3-CT-2002-01810 to G.J.A.R.); the Netherlands Organisation for Scientific Research, NWO (051.04.090 to G.J.A.R.); the Swiss National Science Foundation and the National Competence Center for Research (NCCR) 'Neural Plasticity and Repair' (to H.P.L. and D.P.W.).

REFERENCES

1. Schmidt, A. and Hall, A. (2002) Guanine nucleotide exchange factors for Rho GTPases: turning on the switch. *Genes Dev.*, **16**, 1587–1609.
2. Bernards, A. and Settleman, J. (2004) GAP control: regulating the regulators of small GTPases. *Trends Cell Biol.*, **14**, 377–385.
3. Hall, A. (1998) Rho GTPases and the actin cytoskeleton. *Science*, **279**, 509–514.
4. Van Aelst, L. and D'Souza-Schorey, C. (1997) Rho GTPases and signaling networks. *Genes Dev.*, **11**, 2295–2322.
5. Govek, E.E., Newey, S.E. and Van Aelst, L. (2005) The role of the Rho GTPases in neuronal development. *Genes Dev.*, **19**, 1–49.
6. Luo, L. (2002) Actin cytoskeleton regulation in neuronal morphogenesis and structural plasticity. *Annu. Rev. Cell Dev. Biol.*, **18**, 601–635.
7. Matus, A. (2000) Actin-based plasticity in dendritic spines. *Science*, **290**, 754–758.
8. Tada, T. and Sheng, M. (2006) Molecular mechanisms of dendritic spine morphogenesis. *Curr. Opin. Neurobiol.*, **16**, 95–101.
9. Van Aelst, L. and Cline, H.T. (2004) Rho GTPases and activity-dependent dendrite development. *Curr. Opin. Neurobiol.*, **14**, 297–304.
10. Nadif Kasri, N. and Van Aelst, L. (2008) Rho-linked genes and neurological disorders. *Pflugers Arch.*, **455**, 787–797.
11. Newey, S.E., Velamoor, V., Govek, E.E. and Van Aelst, L. (2005) Rho GTPases, dendritic structure, and mental retardation. *J. Neurobiol.*, **64**, 58–74.
12. Ramakers, G.J. (2002) Rho proteins, mental retardation and the cellular basis of cognition. *Trends Neurosci.*, **25**, 191–199.
13. Chiurazzi, P. and Oostra, B.A. (2000) Genetics of mental retardation. *Curr. Opin. Pediatr.*, **12**, 529–535.

14. van Galen, E.J. and Ramakers, G.J. (2005) Rho proteins, mental retardation and the neurobiological basis of intelligence. *Prog. Brain Res.*, **147**, 295–317.
15. Dierssen, M. and Ramakers, G.J. (2006) Dendritic pathology in mental retardation: from molecular genetics to neurobiology. *Genes Brain Behav.*, **5**(Suppl. 2), 48–60.
16. Kaufmann, W.E. and Moser, H.W. (2000) Dendritic anomalies in disorders associated with mental retardation. *Cereb. Cortex*, **10**, 981–991.
17. Allen, K.M., Gleeson, J.G., Bagrodia, S., Partington, M.W., MacMillan, J.C., Cerione, R.A., Mulley, J.C. and Walsh, C.A. (1998) PAK3 mutation in nonsyndromic X-linked mental retardation. *Nat. Genet.*, **20**, 25–30.
18. Billuart, P., Bienvenu, T., Ronce, N., des Portes, V., Vinet, M.C., Zemni, R., Carrie, A., Beldjord, C., Kahn, A., Moraine, C. *et al*. (1998) Oligophrenin 1 encodes a rho-GAP protein involved in X-linked mental retardation. *Pathol. Biol. (Paris)*, **46**, 678.
19. Harvey, K., Duguid, I.C., Alldred, M.J., Beatty, S.E., Ward, H., Keep, N.H., Lingenfelter, S.E., Pearce, B.R., Lundgren, J., Owen, M.J. *et al*. (2004) The GDP-GTP exchange factor collybistin: an essential determinant of neuronal gephyrin clustering. *J. Neurosci.*, **24**, 5816–5826.
20. Kalscheuer, V.M., Musante, L., Fang, C., Hoffmann, K., Fuchs, C., Carta, E., Deas, E., Venkateswarlu, K., Menzel, C., Ullmann, R. *et al*. (2009) A balanced chromosomal translocation disrupting ARHGEF9 is associated with epilepsy, anxiety, aggression, and mental retardation. *Hum. Mutat.*, **30**, 61–68.
21. Kutsche, K., Yntema, H., Brandt, A., Jantke, I., Nothwang, H.G., Orth, U., Boavida, M.G., David, D., Chelly, J., Fryns, J.P. *et al*. (2000) Mutations in ARHGEF6, encoding a guanine nucleotide exchange factor for Rho GTPases, in patients with X-linked mental retardation. *Nat. Genet.*, **26**, 247–250.
22. Marco, E.J., Abidi, F.E., Bristow, J., Dean, W.B., Cotter, P., Jeremy, R.J., Schwartz, C.E. and Sherr, E.H. (2008) ARHGEF9 disruption in a female patient is associated with X linked mental retardation and sensory hyperarousal. *J. Med. Genet.*, **45**, 100–105.
23. Pasteris, N.G., Cadle, A., Logie, L.J., Porteous, M.E., Schwartz, C.E., Stevenson, R.E., Glover, T.W., Wilroy, R.S. and Gorski, J.L. (1994) Isolation and characterization of the faciogenital dysplasia (Aarskog-Scott syndrome) gene: a putative Rho/Rac guanine nucleotide exchange factor. *Cell*, **79**, 669–678.
24. Bokoch, G.M. (2003) Biology of the p21-activated kinases. *Annu. Rev. Biochem.*, **72**, 743–781.
25. Olson, M.F., Pasteris, N.G., Gorski, J.L. and Hall, A. (1996) Faciogenital dysplasia protein (FGD1) and Vav, two related proteins required for normal embryonic development, are upstream regulators of Rho GTPases. *Curr. Biol.*, **6**, 1628–1633.
26. Reid, T., Bathoorn, A., Ahmadian, M.R. and Collard, J.G. (1999) Identification and characterization of hPEM-2, a guanine nucleotide exchange factor specific for Cdc42. *J. Biol. Chem.*, **274**, 33587–33593.
27. Manser, E., Loo, T.H., Koh, C.G., Zhao, Z.S., Chen, X.Q., Tan, L., Tan, I., Leung, T. and Lim, L. (1998) PAK kinases are directly coupled to the PIX family of nucleotide exchange factors. *Mol. Cell*, **1**, 183–192.
28. Bagrodia, S., Bailey, D., Lenard, Z., Hart, M., Guan, J.L., Premont, R.T., Taylor, S.J. and Cerione, R.A. (1999) A tyrosine-phosphorylated protein that binds to an important regulatory region on the cool family of p21-activated kinase-binding proteins. *J. Biol. Chem.*, **274**, 22393–22400.
29. Baird, D., Feng, Q. and Cerione, R.A. (2005) The Cool-2/alpha-Pix protein mediates a Cdc42-Rac signaling cascade. *Curr. Biol.*, **15**, 1–10.
30. Feng, Q., Albeck, J.G., Cerione, R.A. and Yang, W. (2002) Regulation of the Cool/Pix proteins: key binding partners of the Cdc42/Rac targets, the p21-activated kinases. *J. Biol. Chem.*, **277**, 5644–5650.
31. Feng, Q., Baird, D. and Cerione, R.A. (2004) Novel regulatory mechanisms for the Dbl family guanine nucleotide exchange factor Cool-2/alpha-Pix. *EMBO J.*, **23**, 3492–3504.
32. Koh, C.G., Manser, E., Zhao, Z.S., Ng, C.P. and Lim, L. (2001) Beta1PIX, the PAK-interacting exchange factor, requires localization via a coiled-coil region to promote microvillus-like structures and membrane ruffles. *J. Cell Sci.*, **114**, 4239–4251.
33. Li, Z., Hannigan, M., Mo, Z., Liu, B., Lu, W., Wu, Y., Smrcka, A.V., Wu, G., Li, L., Liu, M. *et al*. (2003) Directional sensing requires G beta gamma-mediated PAK1 and PIX alpha-dependent activation of Cdc42. *Cell*, **114**, 215–227.
34. Yoshii, S., Tanaka, M., Otsuki, Y., Wang, D.Y., Guo, R.J., Zhu, Y., Takeda, R., Hanai, H., Kaneko, E. and Sugimura, H. (1999) alphaPIX nucleotide exchange factor is activated by interaction with phosphatidylinositol 3-kinase. *Oncogene*, **18**, 5680–5690.
35. Node-Langlois, R., Muller, D. and Boda, B. (2006) Sequential implication of the mental retardation proteins ARHGEF6 and PAK3 in spine morphogenesis. *J. Cell Sci.*, **119**, 4986–4993.
36. Neves, G., Cooke, S.F. and Bliss, T.V. (2008) Synaptic plasticity, memory and the hippocampus: a neural network approach to causality. *Nat. Rev. Neurosci.*, **9**, 65–75.
37. Kohn, M., Steinbach, P., Hameister, H. and Kehrer-Sawatzki, H. (2004) A comparative expression analysis of four MRX genes regulating intracellular signalling via small GTPases. *Eur. J. Hum. Genet.*, **12**, 29–37.
38. Bliss, T.V. and Collingridge, G.L. (1993) A synaptic model of memory: long-term potentiation in the hippocampus. *Nature*, **361**, 31–39.
39. Malenka, R.C. and Nicoll, R.A. (1999) Long-term potentiation—a decade of progress? *Science*, **285**, 1870–1874.
40. Kim, J.J., Foy, M.R. and Thompson, R.F. (1996) Behavioral stress modifies hippocampal plasticity through N-methyl-D-aspartate receptor activation. *Proc. Natl Acad. Sci. USA*, **93**, 4750–4753.
41. Wong, T.P., Howland, J.G., Robillard, J.M., Ge, Y., Yu, W., Titterness, A.K., Brebner, K., Liu, L., Weinberg, J., Christie, B.R. *et al*. (2007) Hippocampal long-term depression mediates acute stress-induced spatial memory retrieval impairment. *Proc. Natl Acad. Sci. USA*, **104**, 11471–11476.
42. Xu, L., Anwyl, R. and Rowan, M.J. (1997) Behavioural stress facilitates the induction of long-term depression in the hippocampus. *Nature*, **387**, 497–500.
43. Kim, M.H., Choi, J., Yang, J., Chung, W., Kim, J.H., Paik, S.K., Kim, K., Han, S., Won, H., Bae, Y.S. *et al*. (2009) Enhanced NMDA receptor-mediated synaptic transmission, enhanced long-term potentiation, and impaired learning and memory in mice lacking IRSp53. *J. Neurosci.*, **29**, 1586–1595.
44. Malenka, R.C. and Bear, M.F. (2004) LTP and LTD: an embarrassment of riches. *Neuron*, **44**, 5–21.
45. Gallagher, M., Burwell, R. and Burchinal, M. (1993) Severity of spatial learning impairment in aging: development of a learning index for performance in the Morris water maze. *Behav. Neurosci.*, **107**, 618–626.
46. Whishaw, I.Q. (1985) Cholinergic receptor blockade in the rat impairs locale but not taxon strategies for place navigation in a swimming pool. *Behav. Neurosci.*, **99**, 979–1005.
47. Boda, B., Alberi, S., Nikonenko, I., Node-Langlois, R., Jourdain, P., Moosmayer, M., Parisi-Jourdain, L. and Muller, D. (2004) The mental retardation protein PAK3 contributes to synapse formation and plasticity in hippocampus. *J. Neurosci.*, **24**, 10816–10825.
48. Govek, E.E., Newey, S.E., Akerman, C.J., Cross, J.R., Van der Veken, L. and Van Aelst, L. (2004) The X-linked mental retardation protein oligophrenin-1 is required for dendritic spine morphogenesis. *Nat. Neurosci.*, **7**, 364–372.
49. Khelfaoui, M., Denis, C., van Galen, E., de Bock, F., Schmitt, A., Houbron, C., Morice, E., Giros, B., Ramakers, G., Fagni, L. *et al*. (2007) Loss of X-linked mental retardation gene oligophrenin1 in mice impairs spatial memory and leads to ventricular enlargement and dendritic spine immaturity. *J. Neurosci.*, **27**, 9439–9450.
50. Meng, J., Meng, Y., Hanna, A., Janus, C. and Jia, Z. (2005) Abnormal long-lasting synaptic plasticity and cognition in mice lacking the mental retardation gene Pak3. *J. Neurosci.*, **25**, 6641–6650.
51. McClelland, A.C., Hruska, M., Coenen, A.J., Henkemeyer, M. and Dalva, M.B. (2010) Trans-synaptic EphB2-ephrin-B3 interaction regulates excitatory synapse density by inhibition of postsynaptic MAPK signaling. *Proc. Natl Acad. Sci. USA*, **107**, 8830–8835.
52. Butler, M.G., Dasouki, M.J., Zhou, X.P., Talebizadeh, Z., Brown, M., Takahashi, T.N., Miles, J.H., Wang, C.H., Stratton, R., Pilarski, R. *et al*. (2005) Subset of individuals with autism spectrum disorders and extreme macrocephaly associated with germline PTEN tumour suppressor gene mutations. *J. Med. Genet.*, **42**, 318–321.
53. Kwon, C.H., Luikart, B.W., Powell, C.M., Zhou, J., Matheny, S.A., Zhang, W., Li, Y., Baker, S.J. and Parada, L.F. (2006) Pten regulates neuronal arborization and social interaction in mice. *Neuron*, **50**, 377–388.
54. Cline, H.T. (2001) Dendritic arbor development and synaptogenesis. *Curr. Opin. Neurobiol.*, **11**, 118–126.
55. Poirier, R., Jacquot, S., Vaillend, C., Soutthiphong, A.A., Libbey, M., Davis, S., Laroche, S., Hanauer, A., Welzl, H., Lipp, H.P. *et al*. (2007) Deletion of the Coffin-Lowry syndrome gene Rsk2 in mice is associated

with impaired spatial learning and reduced control of exploratory behavior. *Behav. Genet.*, **37**, 31–50.
56. Hessl, D., Glaser, B., Dyer-Friedman, J. and Reiss, A.L. (2006) Social behavior and cortisol reactivity in children with fragile X syndrome. *J. Child Psychol. Psychiatry*, **47**, 602–610.
57. Mazzocco, M.M. (2000) Advances in research on the fragile X syndrome. *Ment. Retard. Dev. Disabil. Res. Rev.*, **6**, 96–106.
58. Wilding, J., Cornish, K. and Munir, F. (2002) Further delineation of the executive deficit in males with fragile-X syndrome. *Neuropsychologia*, **40**, 1343–1349.
59. Murray, H.J. and O'Connor, J.J. (2004) A role for monomeric G-proteins in synaptic plasticity in the rat dentate gyrus *in vitro*. *Brain Res.*, **1000**, 85–91.
60. Diana, G., Valentini, G., Travaglione, S., Falzano, L., Pieri, M., Zona, C., Meschini, S., Fabbri, A. and Fiorentini, C. (2007) Enhancement of learning and memory after activation of cerebral Rho GTPases. *Proc. Natl Acad. Sci. USA*, **104**, 636–641.
61. Pavlowsky, A., Gianfelice, A., Pallotto, M., Zanchi, A., Vara, H., Khelfaoui, M., Valnegri, P., Rezai, X., Bassani, S., Brambilla, D. *et al*. (2010) A postsynaptic signaling pathway that may account for the cognitive defect due to IL1RAPL1 mutation. *Curr. Biol.*, **20**, 103–115.
62. Nadif Kasri, N., Nakano-Kobayashi, A., Malinow, R., Li, B. and Van Aelst, L. (2009) The Rho-linked mental retardation protein oligophrenin-1 controls synapse maturation and plasticity by stabilizing AMPA receptors. *Genes Dev.*, **23**, 1289–1302.
63. Ridley, A.J. (2006) Rho GTPases and actin dynamics in membrane protrusions and vesicle trafficking. *Trends Cell Biol.*, **16**, 522–529.
64. Kaneko, T., Maeda, A., Takefuji, M., Aoyama, H., Nakayama, M., Kawabata, S., Kawano, Y., Iwamatsu, A., Amano, M. and Kaibuchi, K. (2005) Rho mediates endocytosis of epidermal growth factor receptor through phosphorylation of endophilin A1 by Rho-kinase. *Genes Cells*, **10**, 973–987.
65. Lamaze, C., Chuang, T.H., Terlecky, L.J., Bokoch, G.M. and Schmid, S.L. (1996) Regulation of receptor-mediated endocytosis by Rho and Rac. *Nature*, **382**, 177–179.
66. Khelfaoui, M., Pavlowsky, A., Powell, A.D., Valnegri, P., Cheong, K.W., Blandin, Y., Passafaro, M., Jefferys, J.G., Chelly, J. and Billuart, P. (2009) Inhibition of RhoA pathway rescues the endocytosis defects in Oligophrenin1 mouse model of mental retardation. *Hum. Mol. Genet.*, **18**, 2575–2583.
67. Nakano-Kobayashi, A., Kasri, N.N., Newey, S.E. and Van Aelst, L. (2009) The Rho-linked mental retardation protein OPHN1 controls synaptic vesicle endocytosis via endophilin A1. *Curr. Biol.*, **19**, 1133–1139.
68. Flanders, J.A., Feng, Q., Bagrodia, S., Laux, M.T., Singavarapu, A. and Cerione, R.A. (2003) The Cbl proteins are binding partners for the Cool/Pix family of p21-activated kinase-binding proteins. *FEBS Lett.*, **550**, 119–123.
69. Sorkin, A. and Goh, L.K. (2009) Endocytosis and intracellular trafficking of ErbBs. *Exp. Cell Res.*, **315**, 683–696.
70. Jozic, D., Cardenes, N., Deribe, Y.L., Moncalian, G., Hoeller, D., Groemping, Y., Dikic, I., Rittinger, K. and Bravo, J. (2005) Cbl promotes clustering of endocytic adaptor proteins. *Nat. Struct. Mol. Biol.*, **12**, 972–979.
71. Wu, W.J., Tu, S. and Cerione, R.A. (2003) Activated Cdc42 sequesters c-Cbl and prevents EGF receptor degradation. *Cell*, **114**, 715–725.
72. Benarroch, E.E. (2007) Rho GTPases: role in dendrite and axonal growth, mental retardation, and axonal regeneration. *Neurology*, **68**, 1315–1318.
73. Missy, K., Hu, B., Schilling, K., Harenberg, A., Sakk, V., Kuchenbecker, K., Kutsche, K. and Fischer, K.D. (2008) AlphaPIX Rho GTPase guanine nucleotide exchange factor regulates lymphocyte functions and antigen receptor signaling. *Mol. Cell Biol.*, **28**, 3776–3789.
74. Glaser, E.M. and Van der Loos, H. (1981) Analysis of thick brain sections by obverse-reverse computer microscopy: application of a new, high clarity Golgi-Nissl stain. *J. Neurosci. Methods*, **4**, 117–125.
75. Glaser, J.R. and Glaser, E.M. (2000) Stereology, morphometry, and mapping: the whole is greater than the sum of its parts. *J. Chem. Neuroanat.*, **20**, 115–126.
76. Gundersen, H.J., Bendtsen, T.F., Korbo, L., Marcussen, N., Moller, A., Nielsen, K., Nyengaard, J.R., Pakkenberg, B., Sorensen, F.B., Vesterby, A. *et al*. (1988) Some new, simple and efficient stereological methods and their use in pathological research and diagnosis. *APMIS*, **96**, 379–394.
77. West, M.J., Slomianka, L. and Gundersen, H.J. (1991) Unbiased stereological estimation of the total number of neurons in thesubdivisions of the rat hippocampus using the optical fractionator. *Anat. Rec.*, **231**, 482–497.
78. Prange-Kiel, J., Rune, G.M. and Leranth, C. (2004) Median raphe mediates estrogenic effects to the hippocampus in female rats. *Eur. J. Neurosci.*, **19**, 309–317.
79. Ishizuka, N., Weber, J. and Amaral, D.G. (1990) Organization of intrahippocampal projections originating from CA3 pyramidal cells in the rat. *J. Com. Neurol.*, **295**, 580–623.
80. Sterio, D.C. (1984) The unbiased estimation of number and sizes of arbitrary particles using the disector. *J. Microsc.*, **134**, 127–136.
81. Braendgaard, H. and Gundersen, H.J.G. (1986) The impact of recent stereological advances on quantitative studies of the nervous system. *J. Neurosci. Methods*, **18**, 39–78.
82. Carlin, R.K., Grab, D.J., Cohen, R.S. and Siekevitz, P. (1980) Isolation and characterization of postsynaptic densities from various brain regions: enrichment of different types of postsynaptic densities. *J. Cell Biol.*, **86**, 831–845.
83. Wolfer, D.P., Madani, R., Valenti, P. and Lipp, H.P. (2001) Extended analysis of path data from mutant mice using the public domain software Wintrack. *Physiol. Behav.*, **73**, 745–753.
84. Mohajeri, M.H., Madani, R., Saini, K., Lipp, H.P., Nitsch, R.M. and Wolfer, D.P. (2004) The impact of genetic background on neurodegeneration and behavior in seizured mice. *Genes Brain Behav.*, **3**, 228–239.
85. Lang, U.E., Wolfer, D.P., Grahammer, F., Strutz-Seebohm, N., Seebohm, G., Lipp, H.P., McCormick, J.A., Hellweg, R., Dawson, K., Wang, J. *et al*. (2006) Reduced locomotion in the serum and glucocorticoid inducible kinase 3 knock out mouse. *Behav. Brain Res.*, **167**, 75–86.
86. Madani, R., Kozlov, S., Akhmedov, A., Cinelli, P., Kinter, J., Lipp, H.P., Sonderegger, P. and Wolfer, D.P. (2003) Impaired explorative behavior and neophobia in genetically modified mice lacking or overexpressing the extracellular serine protease inhibitor neuroserpin. *Mol. Cell Neurosci.*, **23**, 473–494.
87. Dulawa, S.C., Grandy, D.K., Low, M.J., Paulus, M.P. and Geyer, M.A. (1999) Dopamine D4 receptor-knock-Out mice exhibit reduced exploration of novel stimuli. *J. Neurosci.*, **19**, 9550–9556.
88. Drai, D. and Golani, I. (2001) SEE: a tool for the visualization and analysis of rodent exploratory behavior. *Neurosci. Biobehav. Rev.*, **25**, 409–426.
89. Keren, G. and Lewis, C. (1979) Partial omega squared for ANOVA designs. *Educ. Psychol. Measur.*, **39**, 119–128.
90. Benjamini, Y., Drai, D., Elmer, G., Kafkafi, N. and Golani, I. (2001) Controlling the false discovery rate in behavior genetics research. *Behav. Brain Res.*, **125**, 279–284.